Modeling the Planar Rocking of a Rigid Body with Irregular Geometry

M. David Burton[1] and Manolis N. Chatzis[2]

[1]PhD Candidate, Dept. of Engineering Science, University of Oxford, Oxford OX1 3PJ, UK.

E-mail: david.burton@eng.ox.ac.uk

[2]Associate Professor, Dept. of Engineering Science, University of Oxford, Oxford OX1 3PJ, UK.

Corresponding Author. E-mail: manolis.chatzis@eng.ox.ac.uk

ABSTRACT

The non-linear dynamics of rocking rigid bodies with simple geometries such as rectangular blocks and cylinders have been the focus of the rocking community over the last six decades. However, many objects that are prone to rocking or overturning do not conform to such geometries. These objects include museum artifacts and precariously balanced rocks in the natural world. Even in cases where the response of the rocking body is planar, the geometry of the body is much more complicated than the commonly studied geometry of a rocking block or a body with only two rocking corners. This paper introduces a complete model that can examine the planar motion of a body with an irregular in-plane polygonal geometry when subjected to a vibrational excitation utilizing the geometry of the body as an input, e.g., in the form of a stereolithography (STL) file. The model is used for studying the rocking response of an object while taking into account sliding and free flight. The problem is formulated and solved using Newtonian equations of motion and impacts are treated as hard. A robust framework for integrating the occurring discontinuous equations of motion and detecting transitions between patterns of motion and impacts, using Matlab, is presented. Suitably chosen examples demonstrate the importance of accounting for the actual geometry of the rocking body studied, whose dynamic response is substantially richer than an object with simplified geometry.

INTRODUCTION

The dynamics of rocking bodies, i.e. those that are not attached or fastened to their support medium, has been a topic of interest to researchers in the field of earthquake engineering. Such objects may be prone to vibration induced by earthquakes or other excitations. Examples include museum artifacts, precariously balanced rocks (PBRs), computer towers and monitors, storage tanks, bookcases and other shelving, a rocking horse, train cars, and more. Often, the most delicate and culturally important of these objects have irregular geometries with uneven mass distributions. In recent decades, researchers have made considerable progress in understanding the non-linear dynamics of rocking rigid bodies (Housner 1963; Ishiyama 1982; Shenton III and Jones 1991; R. Lipscombe and Pellegrino 1993; Chatzis and Smyth 2012b). However, most previous research is typically focused on bodies with simple geometries such as rectangular blocks (Psycharis and Jennings 1983; Spanos and Koh 1984; Chatzis and Smyth 2012a; Zulli et al. 2012) or cylinders (Srinivasan and Ruina 2008; Koh and Mustafa 1990), with more complicated geometries often being approximated by rectangular shapes (Brune et al. 2007; Shi et al. 1996). Museum artifacts and PBRs are examples of objects which would rarely correspond to regular geometries. Museum artifacts have often been studied but previous models do not consider sliding, free flight, a variable location for the impulse at impact, or the potential for more than two rocking vertices, and some do not consider the in-plane irregular geometry of the artifact simplifying the geometry to that of a rectangular block (Wittich et al. 2016; Spyrakos et al. 2017; Fragiadakis et al. 2020). This paper demonstrates that even when the conditions are such that planar rocking would occur, the irregular geometry of such objects and other factors mentioned above affect their response and therefore must be studied to accurately model their dynamics.

To study the behavior of rocking objects, appropriate mathematical and physical models are required. Housner postulated the first of such models for rocking in 1963, dubbed the inverted pendulum model (IPM), which examined the planar behavior of a rectangular rocking block (Housner 1963). Housner introduced several assumptions in his model including the rocking response being planar, the body and foundation being rigid, the angular momentum of the body being conserved

about the post-impact rocking vertex, and sliding and free flight being neglected. This model allows for a qualitative understanding of the rocking response of a body and is hence still the most popular model in the literature. Several studies on the rocking response of bodies have been conducted using the IPM (Spanos and Koh 1984; Tso and Wong 1989; Yim and Lin 1991).

Researchers have shown that neglecting some of Housner's initial assumptions affect the response of a rocking body in a potentially nonconservative manner. Ishiyama introduced a model that examined both sliding and free flight giving six possible types of motion: rest, slide, rotation, slide rotation, translation jump, and rotation jump, finding that sliding and free flight should both be considered (Ishiyama 1982). Shenton and Jones provided a detailed formulation of a rocking model for rigid bodies accounting for sliding and free flight on which the model introduced in this paper builds (Shenton III and Jones 1991). Lipscombe and Pellegrino showed experimentally and numerically that the transition to free flight of rocking rigid bodies becomes more critical as the blocks become more stocky, i.e. as the distance between the support contacts increases relative to the height of the centroid from the support surface, moreover proving that bouncing and free flight should not be neglected in the solution to the rocking problem (R. Lipscombe and Pellegrino 1993). Rocking studies have also been conducted with deformable bodies (Yim and Chopra 1984; Acikgoz and DeJong 2012), deformable supports (Chatzis and Smyth 2012b; Chatzis and Smyth 2012a; Yim and Chopra 1984; Koh et al. 1986), and three dimensions (Zulli et al. 2012; Chatzis and Smyth 2012a; Chatzis and Smyth 2013). All of these factors were proven to have an important effect on the rocking response. While the deformable models account for sliding, free flight, and energy losses without the need for further explicit assumptions, and can be extended to the case of bodies with irregular geometries, such extension can result in them being more computationally demanding.

Several researchers have made an initial step toward irregular geometries by studying block geometries and including parameters to account for eccentricity in the center of mass compared with the geometric center of the block (Plaut et al. 1996; Zulli et al. 2012; Boroschek and Romo 2004; Arredondo et al. 2017; Abadi et al. 2017). However, these models have omitted sliding and

free flight. Such a treatment does not account for other important consequences of an irregular geometry, such as the existence of multiple potential rocking vertices. A further consequence of multiple rocking vertices in irregular objects is that it becomes difficult to characterize such objects as slender or stocky due to the many equivalent heights and widths for every possible orientation of the body. Al Abadi et al. examined the behavior of blocks with eccentric centroids (Abadi et al. 2017). These studies have shown that bodies with centroidal eccentricity may overturn more easily than their symmetric counterparts but they do not take into account irregular base geometries, i.e. anything other than a flat base with two potential rocking vertices.

Another assumption of the IPM is that the resultant of the vertical impulse at impact occurs at the post-impact rocking vertices. Consequently, the reduction of energy due to an impact is uniquely determined by the geometry of the block (Housner 1963). The same assumption is often used in the literature (Zhang and Makris 2001; Yim et al. 1980; Dimitrakopoulos and DeJong 2012; Voyagaki et al. 2014). However, Chatzis et al. (Chatzis et al. 2017), and later Varkonyi et al. in 3-D (Várkonyi et al. 2021), showed that the location of the vertical impulse for a block does not have to be at the post-impact rocking vertex but is permitted to be between the post-impact rocking vertex and the midpoint of the impacting base. Previous works by the authors have demonstrated that rigid impact models require impact-related parameters to be assumed (Chatzis et al. 2017). This is not the case for DEM models where no such assumptions need to be introduced and impact is handled by the properties of the support medium (Chatzis and Smyth 2012a). In cases where the impact parameters have been assumed correctly for a rigid impact model, the results agree with those of a DEM model, e.g., as shown in (Chatzis and Smyth 2012a) for the case of a body with minimal sliding and free flight on two feet placed on a stiff support medium, the stability diagrams produced are in very good agreement with those predicted by the Inverted Pendulum Model. Nonetheless, in more general cases the impact parameters matter for the response and this will be demonstrated through the use of examples throughout the paper.

Due to the significantly different geometric properties between blocks and objects with irregular geometry and the lack of studies on irregular geometry, this work introduces a model that takes into

account the planar irregular polygonal geometry of a rigid body. The irregularity of the geometry has an obvious and significant effect on the response of bodies which cannot be simplified for both planar and 3-D motions. The 3-D response of rigid bodies with irregular geometries will be the topic of investigation of an upcoming paper. This work will instead focus on bodies whose response can be reasonably approximated as planar due to constraints or the object's out-of-plane geometry. A class of systems that experiences planar rocking consists of objects whose geometry comes from an extrusion in the out-of-plane axis. Such examples are discussed later both theoretically and through examples. Other cases of bodies which would favor a planar response despite their geometry are shown in the following Figure 1.

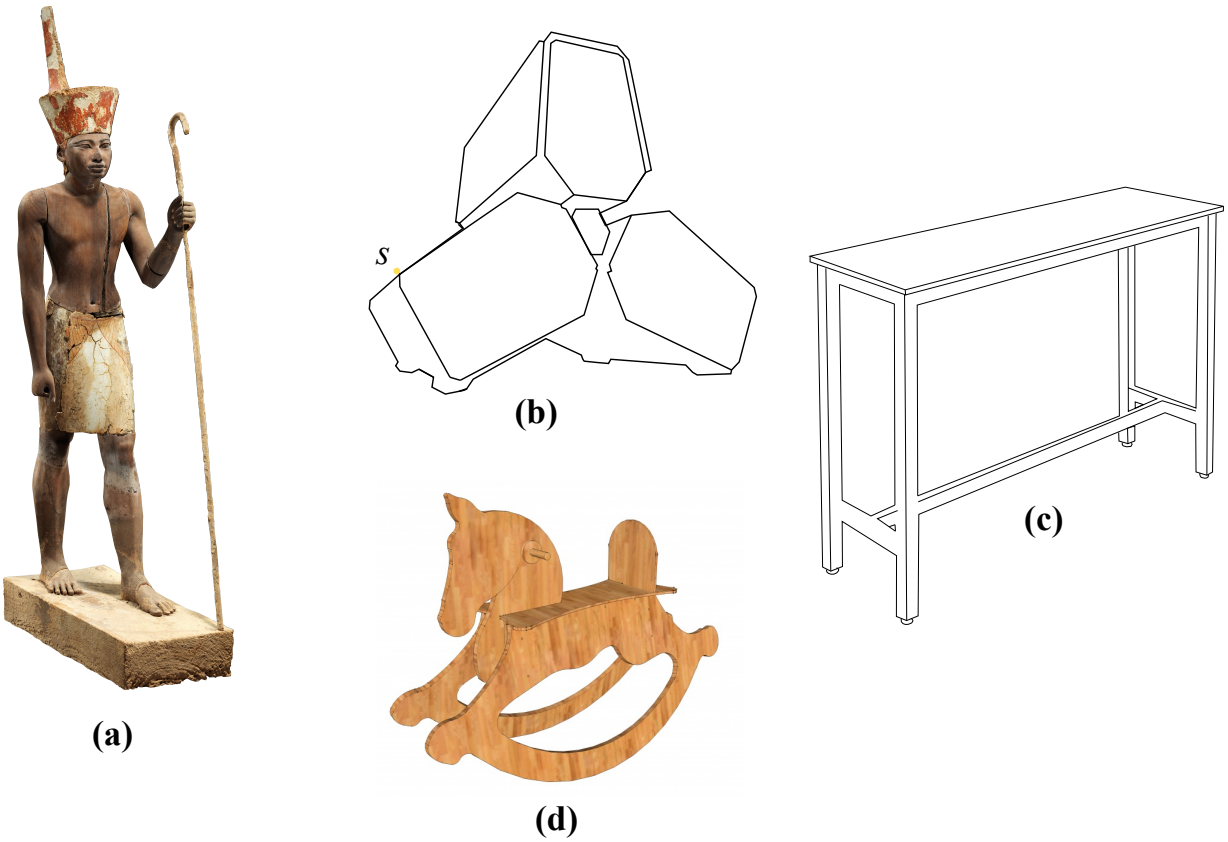

Fig. 1. Objects with irregular geometry which would exhibit planar rocking a) Guardian Figure from the Metropolitan Museum of Art, New York a, b) Sketch of a Computer case b, c) sketch of a table d) a rocking horse d

The computer case of Figure 1b and the table of Figure 1c have a geometry that can be almost

described as an elongated extrusion except of the feet that are placed in the front and back face. The statue of Figure 1a has a base whose length is much larger than its width and is in fact comparable to the estimated height of its centroid. The bodies of Figure 1a-1c would experience practically planar rocking even if left unconstrained. The geometry of interest would be the projection of the overall geometry in the rocking plane.

Finally, Figure 1d shows an example of a rocking horse. This system favors the response in one plane over the other due to the curvature of the contact geometry in one direction that results in a planar response that is usually described as rolling and sliding. Such curved geometries can be approximated as polygonal as discussed in (Burton and Chatzis 2021) and will be the topic of investigation of a future paper.

All the examples studied in this paper have irregular in-plane geometry. The multiple potential rocking vertices and interfaces resulting from such a geometry are taken into account along with sliding and free flight. The geometry of an object is input to the model in the form of a stereolithography (STL) file commonly used in 3-D scanning and printing (Godin et al. 2002). The occurring equations of motion are used to study the dynamic response of objects under support excitations. This allows for the user to obtain dynamic rocking results for any body which will experience planar rocking after specifying the geometry (STL), the density of the body, and the applied excitation. For easier comparison to Shenton and Jones' model and for simplicity, the assumptions of a rigid body and support and planar rocking are retained in this work.

The model includes all possible patterns of motion related to sliding, rocking and free flight. The equations of motion are obtained in a unified manner using a Newtonian formulation and implementation of kinematic constraints for each pattern. The resulting equations are obtained symbolically in Matlab and are integrated numerically using a Runge-Kutta (4-5) formula, the Dormand-Prince pair (Shampine and Gordon 1975; Dormand and Prince 1980), which allows for automated event detection which find the time of transitions between patterns and impacts. Similarly, a unified framework is presented for dealing with impacts, which is capable of handling different post-impact patterns and different assumptions on the location of the vertical impulses

during impact.

Finally, appropriate examples of the code for different irregular objects are presented. These examples include a shelving unit such as those found in warehouses, a precariously balanced rock (PBR), and a museum artifact with useful conclusions being drawn related to the study of irregular geometry, sliding, centroidal eccentricity, various base configurations, and a variable location of the impulse at impact when studying rocking objects.

GENERALIZED COORDINATES

Generally, previous research examined the dynamics of a rectangular block such as the one shown in Figure 2. This rectangular block has half-height h and half-width b. R is the length of the diagonal defined from the rocking vertex p to its centroid c and α is the angle between the long edge and R as shown in Figure 2. The coordinate axes X and Y are defined at the origin o on the support surface. The external forces f_x and f_y are applied at the centroid in the horizontal and vertical directions, respectively.

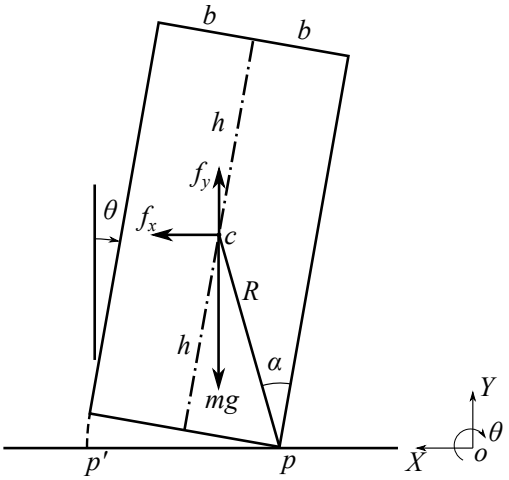

Fig. 2. A rectangular rocking block.

Without any loss of generality, Figure 2 demonstrates the body when it is rocking with respect to the right vertex p. The block has been rotated by an angle θ considered to be positive when clockwise. It is very likely that the weight and external forces applied on the block will cause a

subsequent impact between the body and its support medium, after which the block will rotate about its left rocking vertex p'.

Most models, however, are limited to a rectangular block and do not allow for the analysis of a rigid body with an irregular geometry such as those shown in Figure 1. These bodies have irregular geometry but would also be expected to exhibit planar rocking due to the large length to width ratio of their bases. In the general case, the resulting external geometry of the body when projected in the rocking plane is shown in Figure 3. The position vectors from the centroid c of each of the bodies in Figures 1 and 3 to each rocking vertex, and its angle with a reference axis, are not constant, making this a significantly more complicated problem than the rectangular block.

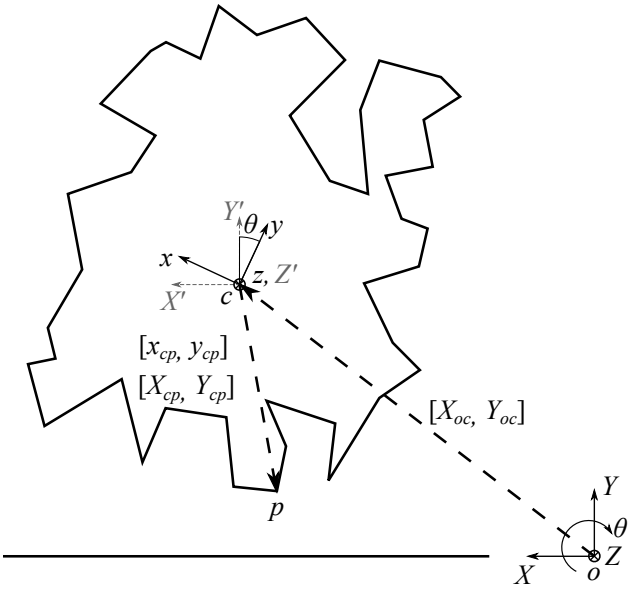

Fig. 3. A rigid body with an irregular in-plane geometry.

A system of Cartesian axes, base S denoted by $oXYZ$, is fixed on an origin o on the support surface as shown in Figure 3. An additional base S', parallel to base S, is fixed at the centroid of the body c with axes $cX'Y'Z'$ and the body has mass m. The Cartesian coefficients of the vector defined from point i to j, $\mathbf{r}_{ij}$, are denoted as the uppercase row vector $[X_{ij},\ Y_{ij},\ Z_{ij}]$. After the calculation of the object's physical parameters as will be discussed in the following section, the third dimension coordinates, Z_{ij}, can be ignored as rocking is constrained to the XY plane. Z_{ij} will normally be omitted from the presented coordinates throughout the paper for conciseness. The

Cartesian coordinates of point i are defined as $[X_{oi},\ Y_{oi}]$. The additional coordinate system, base R denoted by $cxyz$, is fixed on the body. The coefficients of $\mathbf{r}_{ij}$ with respect to the rotating system are defined as the lowercase row vector $[x_{ij},\ y_{ij}]$. Note that for two points p_i and p_j both belonging to the rigid body, the coefficients $[x_{p_ip_j},\ y_{p_ip_j}]$ do not change as the body moves in space. It is convenient to create a registry of the vectors from the centroid to the vertices p_i, $i = 1, ..., N$ for the N vertices of the body.

A rotation matrix, $\mathbf{R}_\theta$, defined in the following equation (1) is used to transform from base R to the Cartesian base S':

$$\mathbf{R}_\theta = \begin{bmatrix} \cos\theta & \sin\theta \\ -\sin\theta & \cos\theta \end{bmatrix} \qquad [X_{ij},\ Y_{ij}] = [x_{ij},\ y_{ij}]\mathbf{R}_\theta \tag{1}$$

The Cartesian coefficients of $\mathbf{r}_{oc}$ are denoted X_{oc} and Y_{oc}. Using the transformations in (1), the Cartesian coordinates of a point, X_{op_i} and Y_{op_i}, can be found as:

$$\begin{aligned} X_{op_i} &= X_{oc} + X_{cp_i} = X_{oc} + x_{cp_i}\cos\theta - y_{cp_i}\sin\theta \\ Y_{op_i} &= Y_{oc} + Y_{cp_i} = Y_{oc} + x_{cp_i}\sin\theta + y_{cp_i}\cos\theta \end{aligned} \tag{2}$$

The Cartesian coefficients of the horizontal and vertical velocities and accelerations of any point, p_i, are then defined as:

$$\begin{aligned} \dot{X}_{op_i} &= \dot{X}_{oc} + \dot{X}_{cp_i} = \dot{X}_{oc} - (x_{cp_i}\sin\theta + y_{cp_i}\cos\theta)\dot{\theta} \\ \dot{Y}_{op_i} &= \dot{Y}_{oc} + \dot{Y}_{cp_i} = \dot{Y}_{oc} + (x_{cp_i}\cos\theta - y_{cp_i}\sin\theta)\dot{\theta} \end{aligned} \tag{3}$$

$$\begin{aligned} \ddot{X}_{op_i} &= \ddot{X}_{oc} + \ddot{X}_{cp_i} = \ddot{X}_{oc} - (x_{cp_i}\sin\theta + y_{cp_i}\cos\theta)\ddot{\theta} - (x_{cp_i}\cos\theta - y_{cp_i}\sin\theta)\dot{\theta}^2 \\ \ddot{Y}_{op_i} &= \ddot{Y}_{oc} + \ddot{Y}_{cp_i} = \ddot{Y}_{oc} + (x_{cp_i}\cos\theta - y_{cp_i}\sin\theta)\ddot{\theta} - (x_{cp_i}\sin\theta + y_{cp_i}\cos\theta)\dot{\theta}^2 \end{aligned} \tag{4}$$

where $\dot{(\cdot)}$ and $\ddot{(\cdot)}$ represents the first and second derivative with respect to time, respectively.

The generalized coordinates that describe the motion of an unconstrained rigid body are thus X_{oc}, Y_{oc}, and θ.

COMPUTATIONAL GEOMETRY FOR AN IRREGULAR BODY

When working with a uniform-density rectangular block, it is straightforward to find the location of c and the inertia tensor $[\boldsymbol{I}]$ about c in base R. However, when the geometry becomes more complicated, a different method is required to find the location of c and $[\boldsymbol{I}]$ of the object. In this work, the starting point is an STL file of an object that would exhibit planar rocking. An example of such an object is shown in Figure 4. The STL file provides the geometry for the studied body. The location of c and the value of $[\boldsymbol{I}]$ must then be derived from the STL. An STL file consists of the 3-D coordinates and a triangulation of the external surface of the 3-D object. It provides a matrix of the x-, y-, and z-coordinates of each vertex on the surface of the object and a connectivity matrix identifying the indices of the three vertices that create each triangle around the exterior of the object (of Congress 2019).

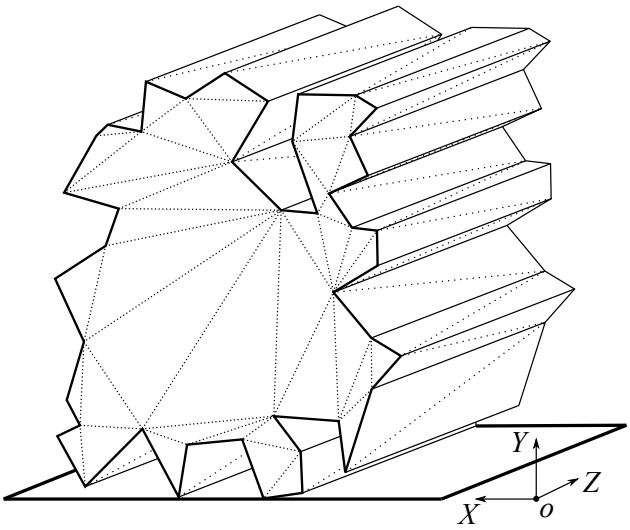

Fig. 4. A 3-D triangulation of a rigid body extruded in the Z-direction.

The flowchart presented in Figure 5 demonstrates the steps required to manage the computational geometry of an irregular body for rocking studies. STL files are easily created in computer aided drafting (CAD) programs or from 3-D scans of existing objects and are initially an ASCII or binary

file. The STL file is imported into Matlab using the stlread function (Johnson 2011) by creating an nx3 matrix $\mathbf{M}_v$ of the n vertex coordinates and an mx3 triangulation matrix $\mathbf{M}_f$ defining the m faces of the object. As the stlread function duplicates many of the object's vertices upon import, the Matlab patchslim function is used to slim the matrices so that each vertex is only listed once in $\mathbf{M}_v$ and the minimum number of faces to completely define the geometry of the body are recorded in $\mathbf{M}_f$ (Esmonde-White 2011). The patchslim function reduces the triangulation to the minimum set of non-overlapping triangles so that every edge of every triangle is only shared by two triangles.

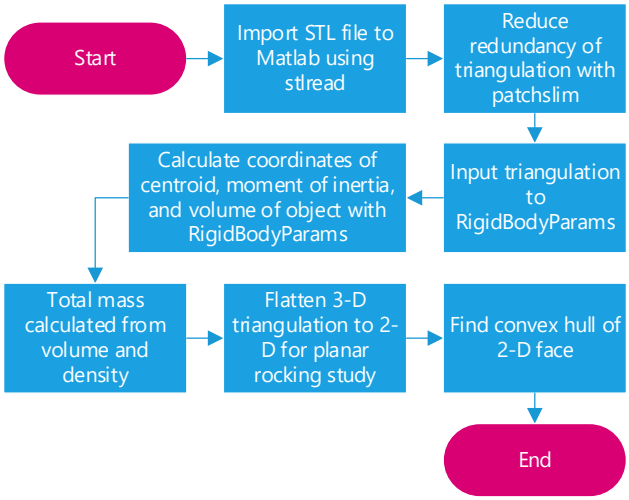

Fig. 5. A flowchart showing the steps required to manage the computational geometry of an irregular, concave body.

To find the location of c, $[\boldsymbol{I}]$, and the volume V of the body, the triangulation from the STL file is supplied to the RigidBodyParams function (Semechko 2019) which uses the divergence theorem (Eberly 2009) to calculate the quantities. A similar procedure is described in Chatzis and Smyth (Chatzis and Smyth 2012a) for calculating penetration volumes and their centroids where the use of the divergence theorem and the related formulas is further explained. As the body is assumed to rotate with respect to the z-axis only, the scalar principal moment of inertia about the z-axis is used as the relevant moment of inertia I_c. If previously unknown, m is found by multiplying V by the density of the body assuming uniform density. The model can also handle objects of nonuniform density by breaking the object into portions of the same density, finding m, V, and the location of c for each portion, and aggregating the results from each portion by weighting each section based

on its total mass to find the location of c and $[\boldsymbol{I}]$ for the whole body.

Only cases of the body experiencing planar rocking are considered in this paper. After calculating V and I_c of the body, the next step is to produce the in-plane geometry which occurs from projecting the original geometry of the body onto the rocking plane. For bodies with uniform geometry, the 2-D projection of the body is used as shown in Figure 4. The examples of this paper consider both extruded geometries and those that vary in the Z direction.

The specific connectivity of the projected vertices is not critical, as the geometry of the rocking system is fully represented by the convex hull of those projected points. The convex hull of a set of points P is the intersection of all convex sets containing P (Weisstein 2019). The contact of the rigid body with a flat horizontal surface can only occur at points which belong to the convex hull of the body. The convex hull of the body in Figure 3 is shown in Figure 6. The most likely point to be in contact with the support surface after rocking begins is the point q_i with the minimum Y-coordinate. When $Y_{oq_i} = 0$ the point q_i is in contact with the support and is thus either a rocking vertex or support contact during the static pattern. Any point on the interior of the blue convex hull polygon cannot touch the support surface regardless of the body's angle of rotation. Only the vertices of the convex hull may become rocking vertices. If any other point of the body was considered as a rocking vertex, then at least one of the vertices of the convex hull would penetrate the support medium, violating the constraints of this model. For the remainder of this paper, the terms vertex, point, or edge refer to a feature of the convex hull.

The vertices of the body belonging to its convex hull will be denoted as q_i and are ordered from 1 to N_c in a counterclockwise manner about the body. The edges of the convex hull E_i are defined as the line segments connecting each convex hull vertex to its adjacent vertices. The body, when in a rocking pattern which will be introduced in Section 4, will only make an impact with the support surface when an edge E_i is parallel to the support surface with a zero Y-coordinate along the entire edge. The angles $\theta_{q_i q_{i+1}}$ between the E_i and the X-axis are calculated for the initial orientation of the body. Figure 6 shows how these angles are defined for an irregular body. Every E_i has a $\theta_{q_i q_{i+1}}$

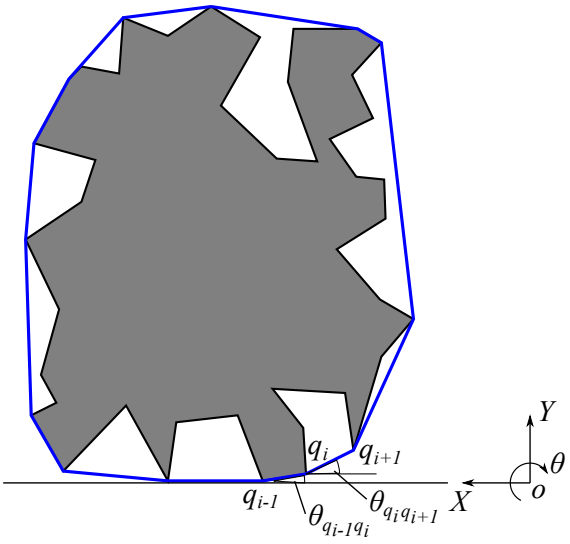

Fig. 6. An irregular body with its convex hull shown and its angles with the horizontal defined.

associated with it. The $\theta_{q_iq_{i+1}}$ are calculated as:

$$\theta_{q_iq_{i+1}} = \text{atan}\left(\frac{y_{q_iq_{i+1}}}{x_{q_iq_{i+1}}}\right) \tag{5}$$

where atan is the four-quadrant inverse tangent based on the coefficients of adjacent convex hull vertices. Matlab's atan2 command is used to find these angles on the closed interval $[-\pi, \pi]$ (The Mathworks). To detect events involving impact, $\theta_{q_iq_{i+1}}$ are then converted to angles on the interval $[0, 2\pi]$. $\theta_{q_iq_{i+1}}$ are compiled into a matrix $\boldsymbol{\theta}_m$ representing the angles at which impact could occur for the body. To allow for the body to undergo more than a full rotation if desired, the angles matrix is expanded:

$$\boldsymbol{\theta}_{m,final} = \boldsymbol{\theta}_m \pm 2\pi n \tag{6}$$

where n is a set of any desired integers and $\boldsymbol{\theta}_{m,final}$ is the matrix used to detect impacts.

EQUATIONS OF MOTION

To determine the motion of an irregular body, the equations of motion must be formulated and solved. Five patterns of motion are defined to model the response of the system, each with its own

kinematic constraints. The patterns can be separated into groups with one, two, or no vertices in contact with the support medium (free flight).

Rocking Patterns

Figure 7 shows an irregular rigid body where only point q_i is in contact with the support surface. In such a case, the body is defined to be in a rocking pattern. The support medium reactions F_x and F_y, horizontal and vertical respectively, act at point q_i as shown, in addition to the external forces f_x and f_y and the force of gravity mg acting at the centroid of the body. The forces F_x, F_y, f_x, and f_y are shown in the positive direction and this convention is applied to all figures in this paper. In the case of the support accelerations studied in this paper, f_x and f_y are D'Alembert forces defined as:

$$f_x = -m\ddot{x}_g \qquad\qquad f_y = -m\ddot{y}_g \tag{7}$$

where $\ddot{x}_g$ and $\ddot{y}_g$ are the horizontal and vertical support accelerations respectively.

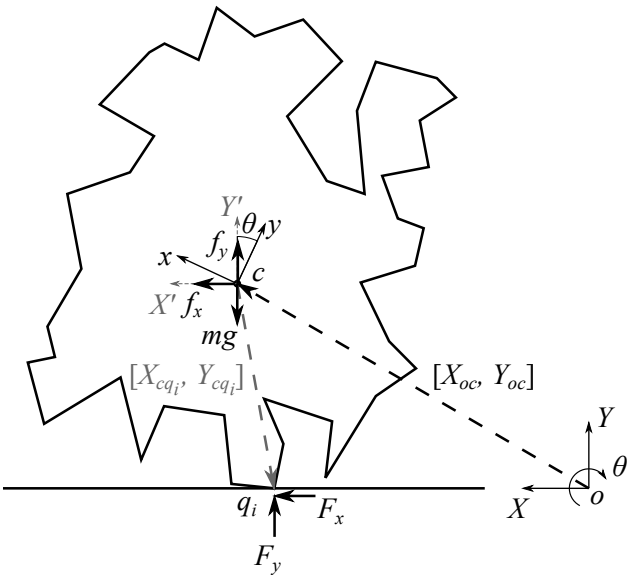

Fig. 7. The forces acting on a rocking rigid body.

Without further assumptions about the constraints that have generated the constraint forces F_x

and F_y, the equations of motion for this body are given in (8).

$$m\ddot{X}_{oc} - F_x = f_x \qquad m\ddot{Y}_{oc} - F_y = f_y - mg \qquad I_c\ddot{\theta} + Y_{cq_i}F_x - X_{cq_i}F_y = 0 \tag{8}$$

The above system of equations has five unknowns: $\ddot{X}_{oc}$, $\ddot{Y}_{oc}$, $\ddot{\theta}$, F_x, and F_y. Two additional equations are thus required to solve the equations of motion. The constraints necessary to solve equation (8) will be defined later in Section 4.

Patterns with Multiple Vertices Contacting Support Medium

The trajectory of the studied system also involves patterns where at least two vertices, q_i and q_{i+1}, are in contact with the support medium as shown in Figure 8.

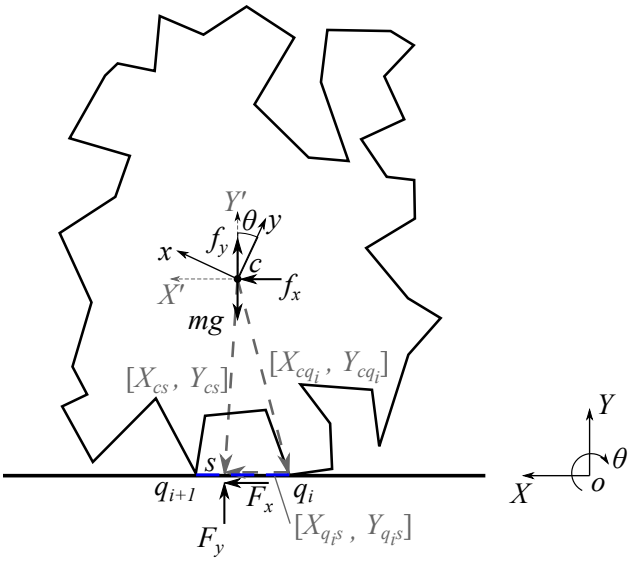

Fig. 8. The vectors and forces relevant to a rigid body in the static pattern or pure sliding with an edge of the convex hull contacting the support surface.

The body could be concave between q_i and q_{i+1}, in which case those are the only points in contact with the support, or it could be a straight edge in which case all the points of the corresponding edge E_i are in contact with the support as represented by the blue dashed line in Figure 8. In either case, the resultant vertical reaction force F_y is applied at a point s between the two vertices q_i and

q_{i+1}. The horizontal Cartesian coordinate of point s is defined by X_{cs} as:

$$X_{cs} = X_{cq_i} + dX_{q_i q_{i+1}} \tag{9}$$

where $d \in [0, 1]$ because the support is assumed to be incapable of providing tensile stresses.

Due to the sixth variable, d, being added for such cases, the equations of motion for these patterns differ from (8). The modified equations of motion are:

$$m\ddot{X}_{oc} - F_x = f_x \qquad m\ddot{Y}_{oc} - F_y = f_y - mg \qquad I_c\ddot{\theta} + Y_{cs}F_x - X_{cs}F_y = 0 \tag{10}$$

The above system has six unknowns: $\ddot{X}_{oc}$, $\ddot{Y}_{oc}$, $\ddot{\theta}$, F_x, F_y, and d, requiring three constraint equations for the unknowns to be determined, which again, are dependent on the pattern of motion and are introduced in Section 4.

Pattern without Contact Points

Figure 9 shows a pattern with no contact between the body and the support medium. In such cases, F_x and F_y are set to zero and the body is only acted on by gravity, f_x, and f_y.

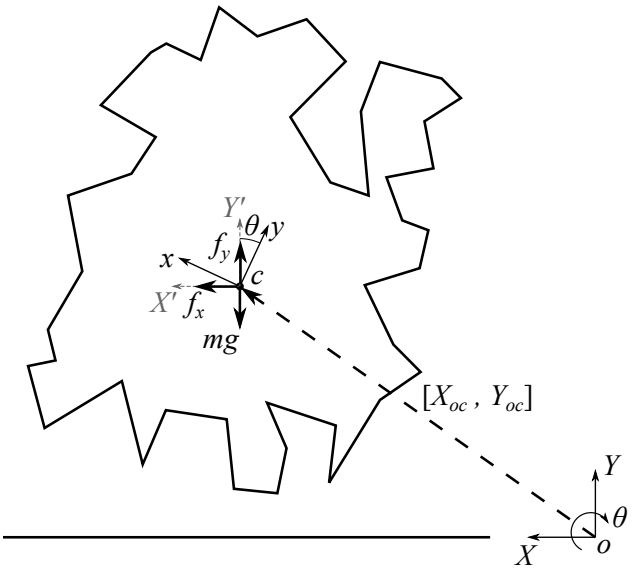

Fig. 9. An irregular body without contact with the support medium and reactions set to zero.

The Patterns of Motion and Their Constraints

There are five possible patterns of motion, as shown in the following Figure 10: the static pattern, pure sliding, pure rocking, slide rocking, and free flight. A different set of independent degrees of freedom (DOFs) is selected for each pattern. This section provides the constraints for each pattern.

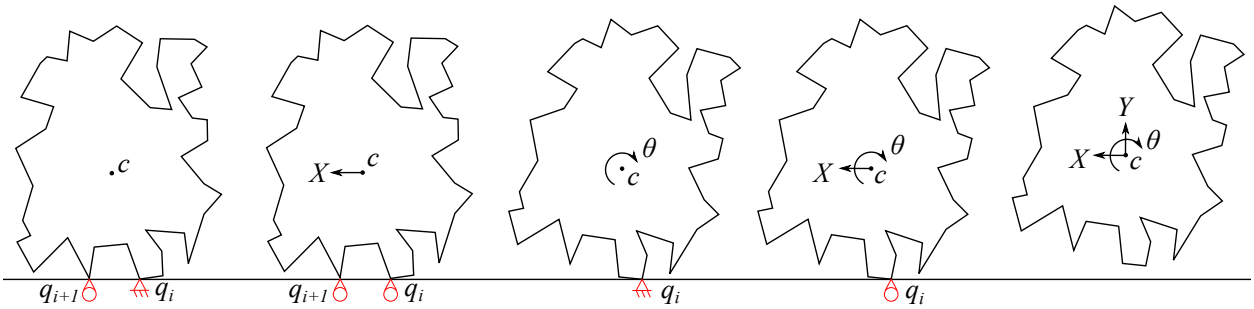

a. Static Pattern b. Pure Sliding c. Pure Rocking d. Slide Rocking e. Free Flight

Fig. 10. The five patterns of motion with their independent DOFs and constraints specified. (a) the static pattern with pin and roller contacts; (b) pure sliding with two rollers; (c) pure rocking with one pin; (d) slide rocking with one roller; (e) Free flight with no contact with the support.

As can be seen in Figure 10a, the static pattern occurs when a body has at least two of its convex hull vertices in contact with the support by a pin in one point (either of the two) and a roller in the other. The kinematic constraints of the static pattern are:

$$\dot{X}_{oq_i} = \ddot{X}_{oq_i} = 0 \qquad \dot{Y}_{oq_i} = \ddot{Y}_{oq_i} = 0 \qquad \dot{Y}_{oq_{i+1}} = \ddot{Y}_{oq_{i+1}} = 0 \tag{11}$$

The velocity constraints in (11) can be integrated to find the additional displacement equations for the static pattern:

$$X_{oq_i} = X_{oq_i}(t_0) \qquad Y_{oq_i} = Y_{oq_i}(t_0) \qquad Y_{oq_{i+1}} = Y_{oq_{i+1}}(t_0) \tag{12}$$

where t_0 is the first time instance the body is in the current static pattern. Likewise, t_0 is defined as the first time instance the body is in the other patterns and is updated for each new instance of each pattern. These equations show that X_{oq_i}, Y_{oq_i}, and $Y_{oq_{i+1}}$ remain constant throughout the static

pattern.

In pure sliding as in Figure 10b, the body has at least two vertices in contact with the support and slides along the support. The constraints for pure sliding are:

$$F_x + \text{sgn}(\dot{X}_{oq_i})\mu F_y = 0 \qquad \dot{Y}_{oq_i} = \ddot{Y}_{oq_i} = 0 \qquad \dot{Y}_{oq_{i+1}} = \ddot{Y}_{oq_{i+1}} = 0 \tag{13}$$

where the first of the above equations is the Coulomb friction law where μ is the coefficient of friction between the body and the support surface and sgn() is the signum function. It should be noticed that $\dot{X}_{oq_i} = \dot{X}_{oq_{i+1}}$. The velocity constraints in (13) can be integrated to obtain the additional pure sliding displacement equations:

$$Y_{oq_i} = Y_{oq_i}(t_0) \qquad Y_{oq_{i+1}} = Y_{oq_{i+1}}(t_0) \tag{14}$$

Pure rocking occurs when only one vertex is in contact with the support and does not slide along the support surface. Two constraint equations are derived from the rocking vertex q_i being restricted from translating in the horizontal and vertical directions (a pinned joint). The kinematic constraints are:

$$\dot{X}_{oq_i} = \ddot{X}_{oq_i} = 0 \qquad \dot{Y}_{oq_i} = \ddot{Y}_{oq_i} = 0 \tag{15}$$

The velocity constraints in (15) can be integrated to find the additional pure rocking displacement equations:

$$X_{oq_i} = X_{oq_i}(t_0) \qquad Y_{oq_i} = Y_{oq_i}(t_0) \tag{16}$$

During slide rocking, the body rotates about a rocking vertex q_i while the same vertex is also permitted to slide along the support surface as shown in Figure 10d. The constraints for slide

rocking are:

$$F_x + \text{sgn}(\dot{X}_{oq_i})\mu F_y = 0 \qquad \dot{Y}_{oq_i} = \ddot{Y}_{oq_i} = 0 \tag{17}$$

The velocity constraint equation in (17) can be integrated to determine the additional slide rocking displacement equation:

$$Y_{oq_i} = Y_{oq_i}(t_0) \tag{18}$$

While in free flight, the body has no contact with the support and the support reactions are set to zero:

$$F_x = 0 \qquad F_y = 0 \tag{19}$$

The Degrees of Freedom and the Equations of Motion

The unconstrained DOFs $\boldsymbol{\Phi}$ and the unconstrained six states, the displacements and velocities for each DOF of the system, $\boldsymbol{Q}$, are:

$$\boldsymbol{\Phi} = \left[X_{oc},\ Y_{oc},\ \theta\right]^T \qquad \boldsymbol{Q} = \left[X_{oc},\ \dot{X}_{oc},\ Y_{oc},\ \dot{Y}_{oc},\ \theta,\ \dot{\theta}\right]^T \tag{20}$$

Due to the constraints mentioned in the previous section, only a subset of $\boldsymbol{\Phi}$ and $\boldsymbol{Q}$ are independent for each pattern. The independent DOFs and the independent states selected to fully describe each pattern are denoted by $\boldsymbol{\Phi}_a$ and $\boldsymbol{Q}_a$ respectively and are summarized in Table 1. The vectors $\boldsymbol{\Phi}_b$ and $\boldsymbol{Q}_b$ represent the remaining dependent DOFs and states of $\boldsymbol{\Phi}$ and $\boldsymbol{Q}$ respectively. Some of the patterns have multiple possible selections for $\boldsymbol{\Phi}_a$ and those shown in Table 1 were selected for their simplicity. The reduction from $\boldsymbol{\Phi}$ to the $\boldsymbol{\Phi}_a$ and their derivatives is necessary to avoid numerical drift during integration and ensure the integration of the equations of motion is computationally efficient.

TABLE 1. Independent Degrees of Freedom and States for Each Pattern

Pattern	Degrees of Freedom, $\boldsymbol{\Phi}_a$	States, $\boldsymbol{Q}_a$
Rest	None	None
Pure Sliding	X	X, $\dot{X}$
Pure Rocking	θ	θ, $\dot{\theta}$
Slide Rocking	X, θ	X, $\dot{X}$, θ, $\dot{\theta}$
Free Flight	X, Y, θ	X, $\dot{X}$, Y, $\dot{Y}$, θ, $\dot{\theta}$

The kinematic equations (2)-(4) are substituted into the constraint equations (11)-(19) as necessary for each pattern. A system of equations is then created for each pattern combining the equations of motion, (8) or (10) depending on the pattern, and the constraint equations with kinematics substituted. This system has the vector of unknowns:

$$\mathbf{V} = \left[\ddot{\boldsymbol{\Phi}}, \boldsymbol{Q}_b, F_x, F_y, d\right]^T \tag{21}$$

where d is only defined for the static pattern and pure sliding. Solving this system of equations results in equations for each of the dependent states $\boldsymbol{Q}_b$ and the reaction variables F_x, F_y, and d.

Thus, the constrained equations of motion for each of the five patterns are formulated symbolically for each of the independent DOFs using Matlab's Symbolic Math Toolbox (MathWorks 2019b). These results are summarized by the following equations:

$$\begin{aligned} \ddot{\boldsymbol{\Phi}}_a &= h(\boldsymbol{Q}_a, m, g, \mu, I_c, x_{cq_i}, y_{cq_i}, \ddot{x}_g, \ddot{y}_g) \\ [F_x, F_y, d] &= j(\boldsymbol{Q}_a, m, g, \mu, I_c, x_{cq_i}, y_{cq_i}, \ddot{x}_g, \ddot{y}_g) \\ \boldsymbol{Q}_b &= k(\boldsymbol{Q}_a, m, g, \mu, I_c, x_{cq_i}, y_{cq_i}, \ddot{x}_g, \ddot{y}_g) \end{aligned} \tag{22}$$

where h, j, and k are the general forms of the non-linear functions occurring after the above process is completed. The right side of these equations are converted to automatically-generated scripts using matlabFunctions (MathWorks 2019a) with the left side as the outputs. These functions are generated once and then used every time the code is run, i.e., they are generated in an offline manner.

k in (22) is the general form of the function that calculates $\boldsymbol{Q}_b$ for any time instance and j is

the general form of the function that is used to calculate F_x, F_y, (and d where necessary), for any time instance during integration. The equations of motion for each pattern from (22) are brought into state-space form using the independent DOFs and states for each pattern:

$$\dot{\boldsymbol{Q}}_a = \begin{bmatrix} \dot{\boldsymbol{\Phi}}_a \\ \ddot{\boldsymbol{\Phi}}_a \end{bmatrix} \tag{23}$$

This reduces the differential equation h of (22) from second-order to first-order. $\boldsymbol{Q}_a$ is then found through integration and $\boldsymbol{Q}_b$ is found post-integration with k. The details of numerical integration are discussed in Section 6.

F_x, F_y, and d are used to determine transitions between patterns, which are discussed in Section 5. Each pattern thus has different symbolic expressions for the equations in (22) as $\boldsymbol{Q}_a$ is different for each pattern, but the same method is used for all patterns to determine $\boldsymbol{Q}_a$ and then calculate $\boldsymbol{Q}_b$ post-integration using matlabFunctions. This automated method using Matlab's symbolic toolbox reduces the likelihood of errors in the resulting formulation and allows for a single approach which is easily expanded to any number of objects with any geometry.

To illustrate the above process for the static pattern: the kinematic equations (2)-(4) are substituted into the constraint equations (11) and (12). These are then combined with the equations of motion (10) to create a system of twelve equations with twelve unknowns: $\ddot{\boldsymbol{\Phi}}$, X_{oc}, Y_{oc}, θ, $\dot{X}_{oc}$, $\dot{Y}_{oc}$, $\dot{\theta}$, F_x, F_y, and d. The solution of this system gives $\dot{\boldsymbol{\Phi}} = \ddot{\boldsymbol{\Phi}} = \mathbf{0}$ and $\boldsymbol{\Phi} = \boldsymbol{\Phi}(t_0)$. The same procedure is completed for the other four patterns which results in unique formulations of the equations of motion for each pattern.

TRANSITIONS BETWEEN PATTERNS

Transitions between the above-described patterns occur during the trajectory of the system. They are separated in the following discussion between transitions with impact and without impact.

Transitions Without Impact

Transitions between patterns can occur without impact in several ways which can be summarized by the following transitions: i) contact vertices transitioning between stick, i.e. the horizontal velocity of support contacts equal to zero, and slide, ii) a pattern with at least two vertices in contact with the support moving to a single-contact pattern and iii) the body lifting off the support into free flight.

Transitions from stick to slide occurs when the horizontal support reaction tends toward exceeding Coulomb's friction law:

$$|F_x(t^*)| = \mu F_y(t^*) \tag{24}$$

where t^* is the exact time the transition occurs. The opposite transition, from a sliding pattern to a non-sliding pattern, occurs at time t^* when:

$$\dot{X}_{oq_i} = 0 \tag{25}$$

where q_i is a vertex in contact with the support medium. However, for the body to transition to stick, Coulomb's criterion must further be satisfied at t^*:

$$|F_x(t^*)| \leq \mu F_y(t^*) \tag{26}$$

If the support contact(s) have zero horizontal velocity, $F_x(t^*)$ is calculated by the equations of the corresponding stick pattern after transition, i.e. either the static pattern or pure rocking. If (26) is not met at t^*, then the sliding pattern is continued with $\text{sgn}(\dot{X}_{oq_i})$ set to a value dependent on F_x. This is discussed later along with the transition from stick to slide. This situation is not common, however, and does not occur in any of the examples provided.

The second category of transitions without impact, from multiple contact points to a single contact point, occurs if s, the point of application of the vertical support reaction F_y, coincides with

either outer vertex defining the edge E_i in contact with the support. This transition occurs at the first time instance that either of the following are true:

$$d = 0 \qquad \text{or} \qquad d = 1 \tag{27}$$

Finally, for transitions to free flight, the positive F_y becomes zero:

$$F_y = 0 \tag{28}$$

Based on the previous descriptions, the following transition between patterns can occur without impacts: the static pattern can transition to pure sliding, pure rocking, and free flight. Pure sliding can transition to the static pattern, slide rocking, and free flight. Pure rocking can transition to slide rocking and free flight. And finally, slide rocking can transition to pure rocking and free flight.

When a stick pattern transitions to a sliding pattern without impact at time t^* or (26) is not met during a sliding pattern, $\dot{X}_{oq_i}(t^*) = 0$. This causes a problem in using the equations of motion at the first time instance of the sliding pattern. To avoid the ill-definition of $\text{sgn}(\dot{X}_{oq_i}(t^*))$, the following procedure explained for the transition from pure rocking to slide rocking is followed: Let F_{xPR} be the horizontal reaction predicted by the pure rocking pattern at the time instance of transitioning to slide rocking similar to F_x shown in Figure 7. Note that at the exact time instance of the transition both the pre-transition pattern and slide rocking are applicable. A new variable s_f is defined as

$$s_f = -\text{sgn}(F_{xPR}) \tag{29}$$

The $\text{sgn}(\dot{X}_{oq_i})$ in the relevant equations for pure sliding (11) or, in this case, for slide rocking (17) must be replaced by s_f at time t^*. It is assumed that the motion of the body will cause q_i to move in the opposite direction of the insufficient horizontal friction force last acting on the rocking vertex during pure rocking. The equivalent procedure is followed for the transition from the static pattern to pure sliding.

Transitions with Impact

When a body rocks on one vertex or moves through the air during free flight, another of its vertices q_i will likely make contact with the support medium with $\dot{Y}_{oq_i} < 0$. As the support medium will not allow the point to penetrate its surface, an impact occurs. Capturing the effects of such an impact on the trajectory of a rocking body is an important part of the rocking model. Because the support medium and the body are both considered to be rigid, this impact will be a hard impact, i.e., it will be infinitesimal in duration. At the instance of impact, at least two vertices of the body will be in contact with the support surface when the pre-impact pattern is rocking. For a pre-impact pattern of free flight, only one vertex will be in contact with the support at impact as long as θ is not equal to any of the elements of $\boldsymbol{\theta}_{m,final}$ as defined in (6).

For a pre-impact rocking pattern, an impact occurs when θ is equal to any of the elements of $\boldsymbol{\theta}_{m,final}$ from equation (6) which will hereon be referred to as impact angles. Figure 6 shows how the impact angles are defined for an irregular body. Thus, an impact occurs during rocking when θ is equal to any of the impact angles. Each angle has two possible events associated with it, one for each direction of $\dot{\theta}$. When an impact angle is reached during integration, the post-impact rocking vertex i and its location are automatically determined depending on $\dot{\theta}$. For free flight, the impact event occurs when $Y_{oq_i} = 0$, i.e., at the negative zero-crossing for Y_{oq_i}, for any vertex q_i of the body's convex hull.

Without any loss of generality, the upper diagrams of Figure 11 shows an impact occurring from a pre-impact rocking pattern where the body is shown immediately before, during, and immediately after the impact (from left to right). Initially, the body rocks about p, then impacts at i and begins rocking about i. The pre-impact velocities are denoted by the superscript $^-$ and the post-impact velocities by the superscript $^+$. During the impact, a horizontal impulse J_x and a vertical impulse J_y are applied by the support medium to the body at a point u between the pre- and post-impact rocking vertices p and i respectively. For the case of pre-impact free flight shown in the lower diagram of Figure 11, the object begins in free flight then impacts the support at i which must be the same as u due to it being the only point in contact with the support.

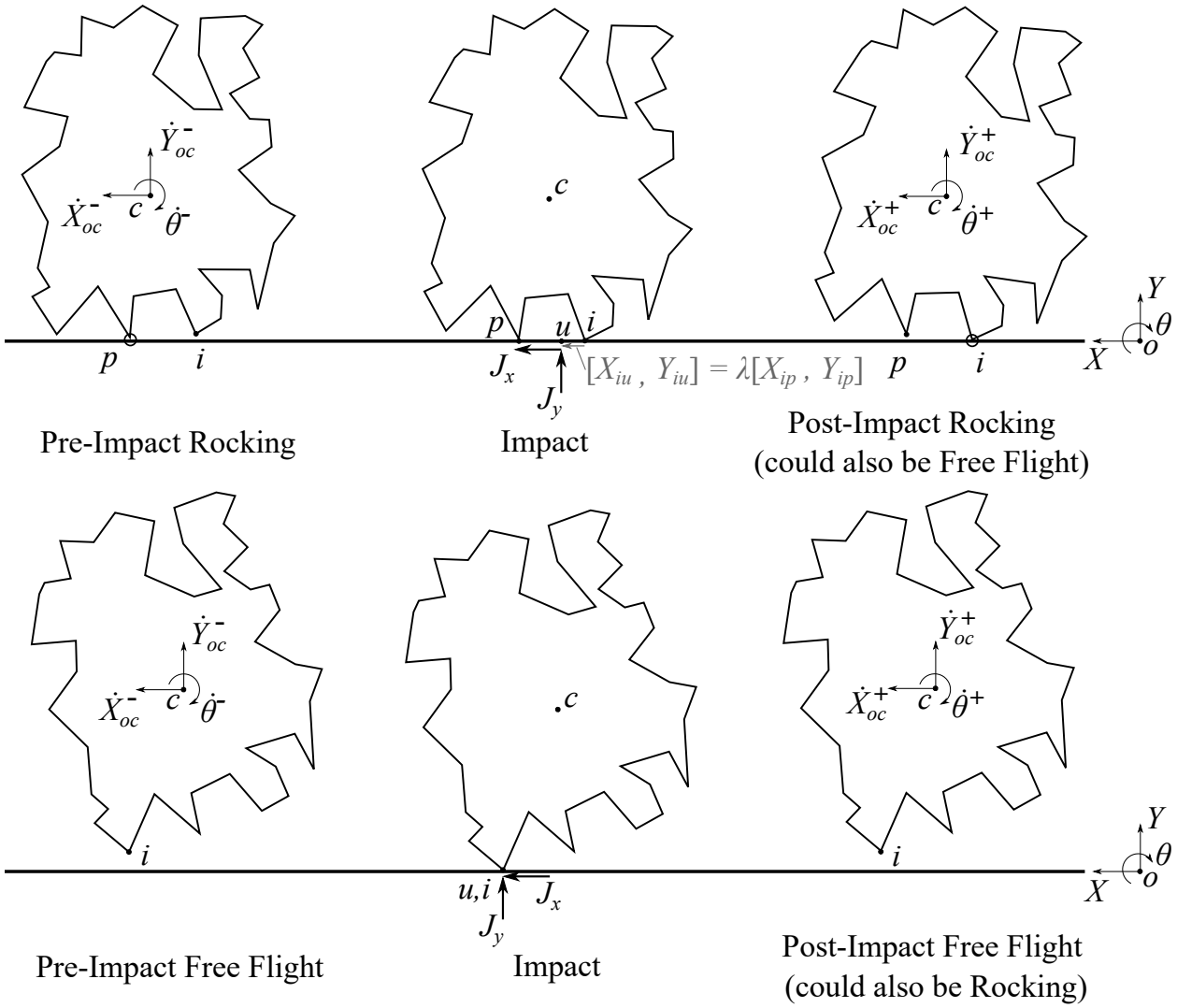

Fig. 11. Upper diagram: From left to right shows an irregular body rocking on p, impacting the support surface, and continuing to rock on i. The open circles indicate the rocking vertices. Lower diagram: From left to right shows an irregular body in free flight, impacting the support surface at i, and returning to free flight. Positive velocity conventions are shown.

The vector $\mathbf{r}_{cu}$ defines the location of u:

$$\mathbf{r}_{cu} = \mathbf{r}_{ci} + \lambda \mathbf{r}_{ip} \tag{30}$$

where λ is a scalar. Due to the inability of the support medium to provide tensile stresses J_y must be applied between i and p, i.e., $\lambda \in [0, 1]$, with $\lambda = 0$ and $\lambda = 1$ corresponding to J_y being applied to i and p respectively. For rectangular blocks and pure rocking, $\lambda \leq 0.5$ is necessary to avoid gain

of energy during the impact as discussed in (Chatzis et al. 2017). For irregular bodies, there is no known explicit limit to λ as the slenderness and different options for pre- and post-impact patterns vary. However, this value can be calculated numerically from the condition that the overall energy of the system is not increased after impact. In the examples provided, the value of λ was monitored so that is does not result in an increase of energy.

For impacts where free flight is the pre-impact pattern, λ does not need to be defined as i and u must be coincidental. It is theoretically possible for an impact from free flight to happen with two or more vertices simultaneously impacting the support, but this is highly unlikely and does not appear in any examples presented in this paper so is thus ignored. Thus, for an impact from free flight:

$$\mathbf{r}_{cu} = \mathbf{r}_{ci} \tag{31}$$

For any impact, four sets of impact conditions are possible. Each of the options places a restriction on the impacting vertex i immediately post-imapct. The four impact conditions are: "pure rocking" where i is restricted from moving in X and Y, "slide rocking" where i may slide but not uplift from the support, "free flight without sliding" where i may uplift from the support but must have $\dot{X}^+_{oi} = 0$, and "free flight without restriction" where i may uplift from the support and move horizontally. This model assumes, as (Shenton III and Jones 1991) does, that the support will cause X^+_{oi} and Y^+_{oi} to be zero if possible. The model thus has the following order of preference for the impact conditions: pure rocking, slide rocking, free flight without sliding, and free flight without restriction. These assumptions are necessary because more than one post-impact pattern may be applicable, with free flight typically being a valid pattern.

The equations of momentum for any body at impact are:

$$m\dot{X}^+_{oc} = m\dot{X}^-_{oc} + J_x \qquad m\dot{Y}^+_{oc} = m\dot{Y}^-_{oc} + J_y \qquad I_c\dot{\theta}^+ = I_c\dot{\theta}^- - Y_{cu}J_x + X_{cu}J_y \tag{32}$$

Therefore, there are six unknowns in three equations: $\dot{X}^+_{oc}$, $\dot{Y}^+_{oc}$, $\dot{\theta}^+$, J_x, J_y, and λ. λ arises from

$X_{cu} = X_{ci} + \lambda X_{ip}$ and must be assumed to reduce the number of unknowns to five. The unknowns in (32) are solved for by using two constraint equations for each post-impact pattern. The constraint equations for impact change depending on the post-impact pattern similar to the constraints for the equations of motion. In all cases, the two post-impact constraints, which are given in (33)-(36) below, and the equations of momentum (32) are combined to create a system with five equations and five unknowns. The system of equations is created and solved in the order of preference described above. The post-impact velocities and impulses obtained for each pattern must then be checked to ensure the solution to the impact is valid as discussed in the following Section 5. If one of the post-impact patterns is valid, the rest of the patterns are not checked and the velocities immediately after impact are defined as the initial conditions for the integration of the post-impact pattern.

For post-impact pure rocking, the constraint equations are:

$$\dot{X}_{oi}^{+} = 0 \Rightarrow \dot{X}_{oc}^{+} = Y_{ci}\dot{\theta}^{+} \qquad \dot{Y}_{oi}^{+} = 0 \Rightarrow \dot{Y}_{oc}^{+} = -X_{ci}\dot{\theta}^{+} \tag{33}$$

The constraint equations for post-impact slide rocking are:

$$J_x = -\text{sgn}(\dot{X}_{oi}^{+})\mu J_y \qquad \dot{Y}_{oi}^{+} = 0 \Rightarrow \dot{Y}_{oc}^{+} = -X_{oi}\dot{\theta}^{+} \tag{34}$$

The constraint equations for post-impact free flight without sliding are:

$$\dot{X}_{oi}^{+} = 0 \Rightarrow \dot{X}_{oc}^{+} = Y_{oi}\dot{\theta}^{+} \qquad \dot{Y}_{oi}^{+} = -\epsilon\dot{Y}_{oi}^{-} \tag{35}$$

where ϵ is a coefficient of restitution defining the ratio of $\dot{Y}_{oi}^{+}$ to $\dot{Y}_{oi}^{-}$. Finally, the constraint equations for free flight without restriction are:

$$J_x = -\text{sgn}(\dot{X}_{oi}^{+})\mu J_y \qquad \dot{Y}_{oi}^{+} = -\epsilon\dot{Y}_{oi}^{-} \tag{36}$$

The acceptable values for ϵ in the above equations theoretically lie on the interval $[0, 1]$ though

the upper bound of 1 may be reduced by the requirement that there be no increase in the body's energy at impact. The energy before and after impact must be checked numerically after each impact. The negative sign in front of ϵ ensures that $\dot{Y}_{oi}^{+}$ is in the opposite direction of $\dot{Y}_{oi}^{-}$.

Validity Conditions for Post-Impact Patterns

The set of conditions required for a valid impact vary for each potential post-impact pattern. For all post-impact patterns the following condition must be true as the support is tensionless and J_y as shown in Figure 11 must therefore be positive:

$$J_y \geq 0 \tag{37}$$

Other conditions are only necessary for certain post-impact patterns. For post-impact rocking from a pre-impact rocking pattern to be valid, $\dot{\theta}^{+}$ must have the same sign as $\dot{\theta}^{-}$ or be equal to zero:

$$\text{sgn}(\dot{\theta}^{+}) = \text{sgn}(\dot{\theta}^{-}) \qquad \text{or} \qquad \dot{\theta}^{+} = 0 \tag{38}$$

If $\text{sgn}(\dot{\theta}^{+}) \neq \text{sgn}(\dot{\theta}^{-})$ for a pre-impact rocking pattern going to a post-impact rocking pattern, a second impact would follow immediately after the first impact without time passing between the two impacts. A very specific value of λ depending on the body geometry would be required to cause $\dot{\theta}^{+} = 0$. Its discussion is provided here for mathematical completeness. This is not possible as was also observed in (Shenton III and Jones 1991). However, if the pre-impact pattern is free flight, condition (38) is not necessary. The sign of $\dot{\theta}$ can change after impact from free flight. Instead of this condition, for pre-impact rocking to post-impact free flight the following condition is necessary:

$$\dot{Y}_{op}^{+} \geq 0 \tag{39}$$

as a negative vertical velocity would cause an impact immediately after the initial impact which is not permitted.

Finally, if the post-impact pattern does not permit sliding, i.e., in the case of post-impact pure rocking and free flight with $\dot{X}_{oi}^{+} = 0$, Coulomb's inequality applied to the impulses must be valid during the impact:

$$|J_x| \leq \mu J_y \tag{40}$$

Otherwise, sliding will occur during impact and as a result $\dot{X}_{oi} \neq 0$. The effect of violating equation (40) is that a pure rocking post-impact pattern is replaced by slide rocking, and a free flight pattern with $\dot{X}_{oi} = 0$ is replaced by free flight with $\dot{X}_{oi} \neq 0$.

Table 2 displays the options for post-impact patterns and the conditions which must be met for each pattern to be valid.

TABLE 2. Conditions for Each Post-Impact Pattern

Condition	Pure Rocking	Slide Rocking	Free Flight without Sliding	Free Flight
$J_y \geq 0$	X	X	X	X
$\text{sgn}(\dot{\theta}^{+}) = \text{sgn}(\dot{\theta}^{-})$ or $\dot{\theta}^{+} = 0$ (for pre-impact rocking only)	X	X		
$\dot{Y}_{op}^{+} \geq 0$ (for pre-impact rocking only)			X	X
$\lvert J_x \rvert \leq \mu J_y$	X		X	

Each of the post-impact patterns are checked in the order presented above. If any of the validity conditions for the pattern are not met, the post-impact pattern is deemed invalid and the next pattern is checked. If at any point, one of the post-impact patterns fulfill all its validity conditions, that pattern is selected as the post-impact pattern and the other less-restrictive options are not checked.

Note the introduction of $\text{sgn}(\dot{X}_{oi}^{+})$ in the friction constraint of equations (34) and (36). The value of $\text{sgn}(\dot{X}_{oi}^{+})$ is unknown prior to solving the momentum equations and therefore requires a guess, $\text{sgn}(\dot{X}_{oi}^{+})_{guess}$, and a check with the resulting value after solving, $\text{sgn}(\dot{X}_{oi}^{+})_{actual}$. The condition:

$$\text{sgn}(\dot{X}_{oi}^{+})_{guess} = \text{sgn}(\dot{X}_{oi}^{+})_{actual} \tag{41}$$

is checked for post-impact slide rocking or free flight with sliding during impact. If equation (41) is not satisfied after the first attempt, $\text{sgn}(\dot{X}_{oi}^{+})_{guess}$ is changed to $\text{sgn}(\dot{X}_{oi}^{+})_{actual}$ and tested again. If equation (41) is still invalid, it does not necessarily constitute an error but it is unknown what value $\text{sgn}(\dot{X}_{oi}^{+})$ should be set for this model. This is a situation beyond the limits of the assumed impulse version of the Coulomb friction model but does not occur commonly in practice. In the examples presented later, this scenario does not occur. If the post-impact slide rocking fails to meet equation (41) twice, the model could be stopped or the free flight checks could be carried out.

Transitions occurring at impacts are explained through the flowchart in Figure 12. This flowchart summarizes the programmatic flow of the model to solve impacts, displaying the order of preference for post-impact patterns. The flowchart also details the conditions needed to validate each post-impact pattern which are dependent on the pre-impact pattern.

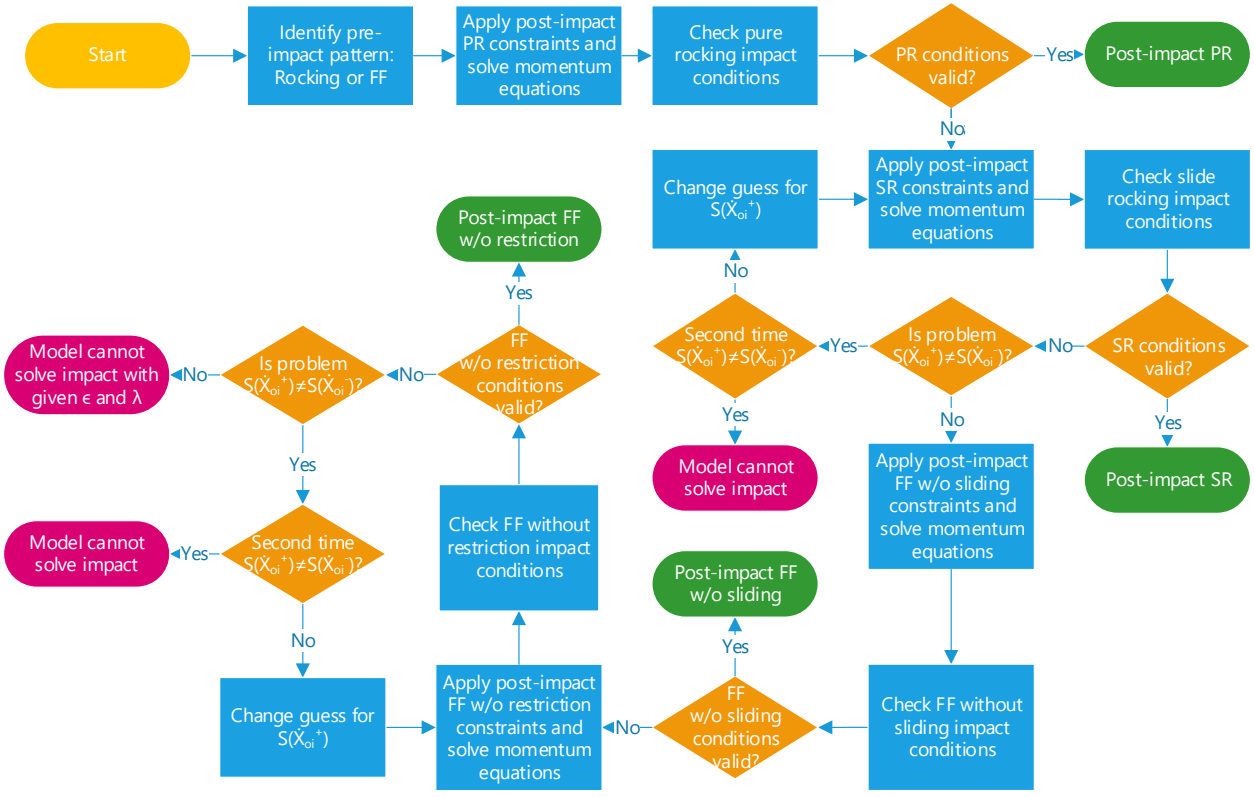

Fig. 12. A flowchart displaying how impacts are handled where PR = Pure Rocking, SR = Slide Rocking, and FF = Free Flight.

If the algorithm reaches free flight, the last post-impact pattern checked, and the results are

still invalid, then the model is not capable of solving that particular impact with the given values of ϵ and λ. Changing the location of the impulse defined by λ changes the post-impact velocities and thus the post-impact pattern can also be affected. Additionally, ϵ can affect the validity of post-impact free flight.

There is a small subset of impacts, depending on the geometry and velocities of the body, where the pre-impact rocking vertex p in a pre-impact rocking pattern violates condition (39) upon solving the equations of momentum. This may occur more frequently for bodies where, at the instance of impact, $|X_{ip}|$ is greater than $|Y_{ic}|$. In this case, there is a problem with either the location of j dictated by λ, the coefficient of restitution ϵ, or the combination of the two as they are arbitrarily defined. Alternate values for λ and/or ϵ can be selected so that $\dot{Y}_{op}^{+} > 0$. Nevertheless, impacts that require a change in ϵ and/or λ are very rare for reasonable initial selections of ϵ and λ and they do not occur in the examples provided.

Energy-Based Transitions

Energy is lost during each impact, through the corresponding momentum equations. However, the energy of the body never becomes zero even after an infinite number of impacts. Numerically, there will be situations where some of the states of interest have practically become very small numbers. A common occurrence is for the magnitude of $\dot{\theta}$ to become very small which leads to the instance of the body experiencing multiple consecutive impacts over a very small time period. Eventually this will lead to $\dot{\theta}$ attaining a value that is comparable to the machine tolerance. If such values are used in the momentum equations, precision errors will be induced potentially leading to an artificial increase of energy in the system and a numerical instability. Instead, it is clear that $\dot{\theta}$ would become zero shortly after this situation is met. To avoid this issue, a reasonably chosen minimum value for $|\dot{\theta}^{+}|$ is selected and if $|\dot{\theta}^{+}|$ falls below the minimum value, the two rocking vertices which were impacting the support are both placed on the support with zero velocity in the static pattern. The same can be true for a slide rocking body, only when $|\dot{\theta}^{+}|$ is negligible, the body is instead forced to pure sliding on the two engaged rocking vertices.

The transition from repeated free flight impacts to a rocking pattern faces the same difficulty as

the transition from rocking to a multi-contact pattern. In some cases the same point i will repeatedly impact the support and $\dot{Y}_{oi}^{+}$ will become smaller and smaller until it reaches the machine tolerance. To avoid this, a reasonably chosen minimum value for $\dot{Y}_{oi}^{+}$ is selected and if $\dot{Y}_{oi}^{+}$ is less than this value the impacting point is transitioned from free flight and placed on the support in a rocking pattern. The new rocking pattern may be either pure or slide rocking, depending on $\dot{X}_{oi}^{+}$ when the transition occurs. If $\dot{X}_{oi}^{+} \neq 0$ the object will enter slide rocking; otherwise it will enter pure rocking.

Summary of Transitions

A summary of the permitted non-impact and energy-based transitions between patterns is shown in Figure 13. The criteria that must be met for one pattern to transition to another is provided along each path between patterns.

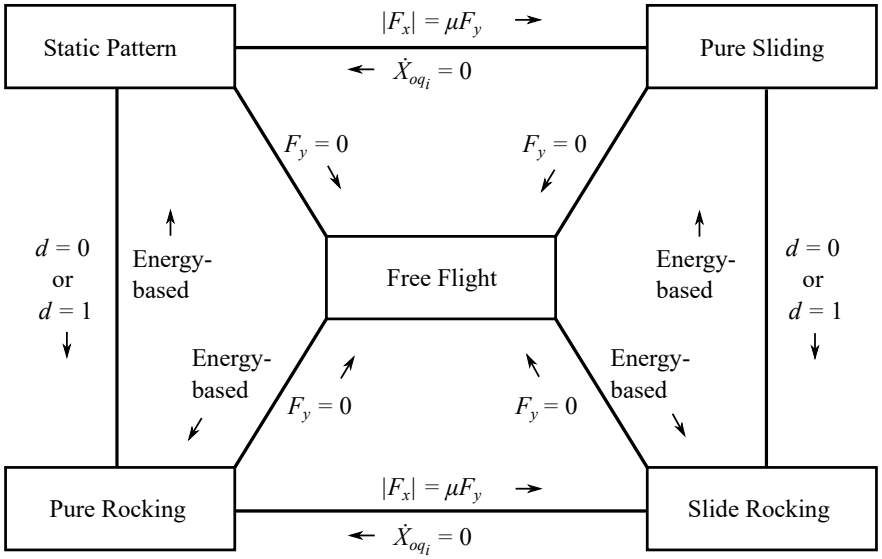

Fig. 13. Diagram showing the non-impact and energy-based transitions between the five patterns of motion.

NUMERICAL INTEGRATION OF THE EQUATIONS OF MOTION

The equation (23) is numerically integrated over time using Matlab's ode45 function. Ode45 uses an explicit Runge-Kutta (4, 5) Dormand-Prince pair (RKDP) to solve the system of first-order ordinary differential equations given the differential equation or system of equations, the time span including the start and end times, and the initial conditions of the differential equations (Shampine

and Gordon 1975). An advantage of using a variable time stepping RKDP is the ability to detect events.

Transitions between patterns and impacts are detected using Matlab's ODE event location option. An event function runs simultaneously with ode45 and stops integration when an event occurs. Determining when an event occurs programmatically is strictly necessary to enable accurate solution. During integration, the event function triggers ode45 to stop integration of a given pattern when the criteria for transition to another pattern or impact are met. If the event is an impact, the equations of momentum are then solved to determine the post-impact velocities. If the event is a non-impact transition derived from equations (24), (25), (27), or (28), the equations of momentum are not evaluated and the required states are sent to the next pattern's integration.

A numerical model is introduced using the methods described above. In addition, a subset of the full model is designed that prohibits sliding or free flight. The model follows the structure found in Figure 14.

EXAMPLES OF THE ROCKING BEHAVIOR OF BODIES WITH IRREGULAR GEOMETRY

In this section a series of examples demonstrate the use of the model. As stated in the the previous sections, the model is applicable to a wide range of bodies which are expected to experience planar rocking and have irregular in-plane geometries. Due to length limitations, the examples only consider some of such cases while emphasizing the effects of sliding, free flight, and the assumptions regarding impact.

Shelving Unit Subjected to Sinusoidal Pulses

Figure 15 shows an example of the in-plane geometry of a shelving unit that would be found in a warehouse or in a residential or office setting on a smaller scale.

The shelving unit is an object whose geometry arises from an extrusion in the Z-direction with an out-of-plane length of 3 meters. A steel unit of this size would present a life safety and property damage risk even without additional content on its shelves if exposed to support accelerations and rocking motion. Four different base configurations are provided to test which configurations offer better stability from support accelerations. The flat base of Figure 15a is the typical flat base used

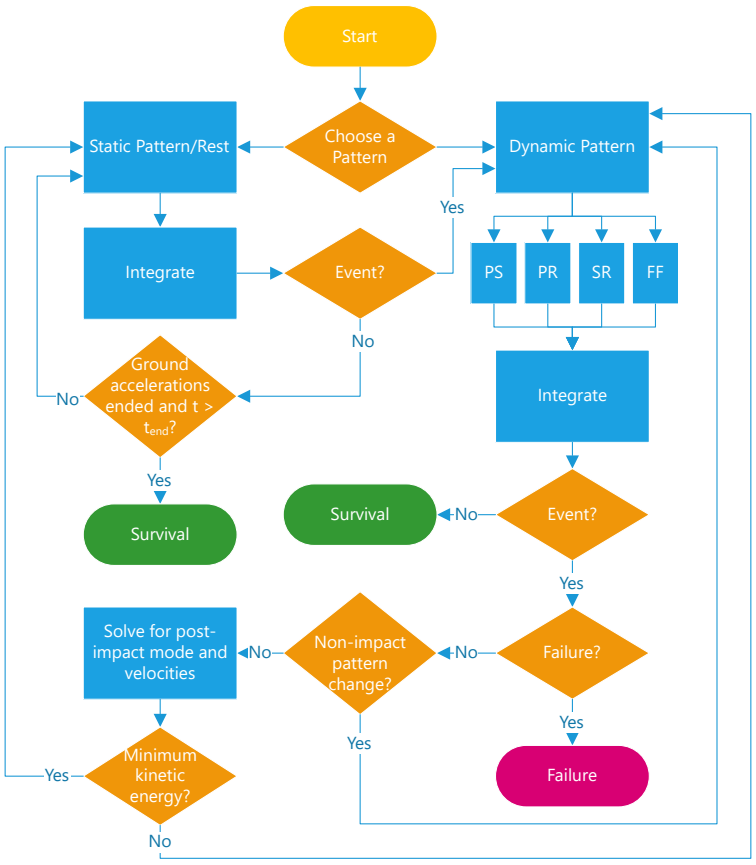

Fig. 14. Flowchart showing the overall structure of the code.

in many rocking studies with two potential rocking vertices. The flat base will be tested with both $\lambda = 0$ and $\lambda = 0.3$ to show the importance of considering this parameter as previously demonstrated in (Chatzis et al. 2018). The other base configurations shown in Figure 15b-d cannot be studied by previous models as they have more than two rocking vertices. The other base configurations use the assumption of $\lambda = 0$ for simplicity, unless noted otherwise. Figure 15b shows a base with quarter circle feet. As shown in the figure, the lowest part of the arcs are below the flat portion of the base to ensure they are the only part of the base to come into contact with the support. Figure 15c has 5 cm extensions on either side of the base at 45 degree angles to the horizontal that will become the rocking vertex if the shelving rotates by about 10 degrees in either direction. Finally, Figure 15d shows the common situation of two slightly uneven rectangular feet on either side of the unit. The foot on the left has a height of 1 cm while that on the right has a height of 2 cm. This results in a slightly askew unit which would make impacts with four vertices on the feet and two

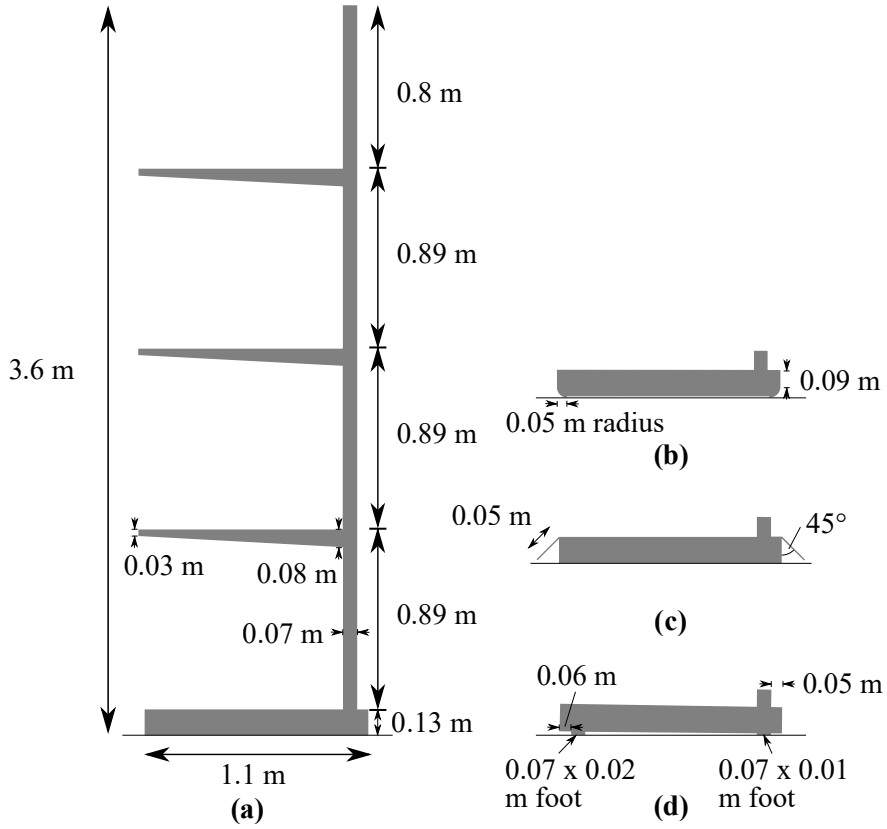

Fig. 15. A shelving unit with several base configurations. a) Flat base. b) Quarter circle feet. c) Extensions on either side. d) Uneven feet perpendicular to the flat base.

additional vertices at the extremities of the base. The STL files for each of these units are provided in STL Files S1 to S4 of the supplementary material.

The horizontal support accelerations applied to the shelving unit, $\ddot{x}_g$, has the form of a sinusoidal pulse of exactly one cycle:

$$\ddot{x}_g = \begin{cases} A\sin(2\pi f t), & \text{if } 0 \le t \le \frac{1}{f} \\ 0, & \text{if } t > \frac{1}{f} \end{cases} \tag{42}$$

where A is the amplitude of the pulse in terms of g, and f is the linear frequency of the pulse in Hz. The vertical support acceleration, $\ddot{y}_g$, is zero throughout the simulations.

For any excitation applied, the occurring time histories of the six states of the system are found. The angles at which the body fails by toppling, were selected to be -1.5 rad and 1.5 rad,

indicating toppling failure. The positive and negative failure limits are referred to as clockwise and counterclockwise failure respectively in the following discussion. If θ never exceeds the failure angles during the pulse and for a reasonable amount of time after the pulse has ended, the body is deemed to have survived the pulse.

To test the broad likelihood of survival or failure for the shelving units and the different base configurations, a range of sinusoidal pulses were applied to each of the models, varying A from $0.01g$ to $3g$ and f from 0.1 to 5 Hz. The result of each pulse is recorded as either survival or failure. The boundaries between survival and failure can then be compiled for each of the configurations into stability diagram such as those shown in Figure 16. The subfigures in Figure 16 correspond to the first local maximum magnitude of the support acceleration having different signs, i.e., a different direction of the pulse. One can track which area corresponds to survival or failure starting from the observation that, as expected, for any value of f, very small values of A result in the body not overturning.

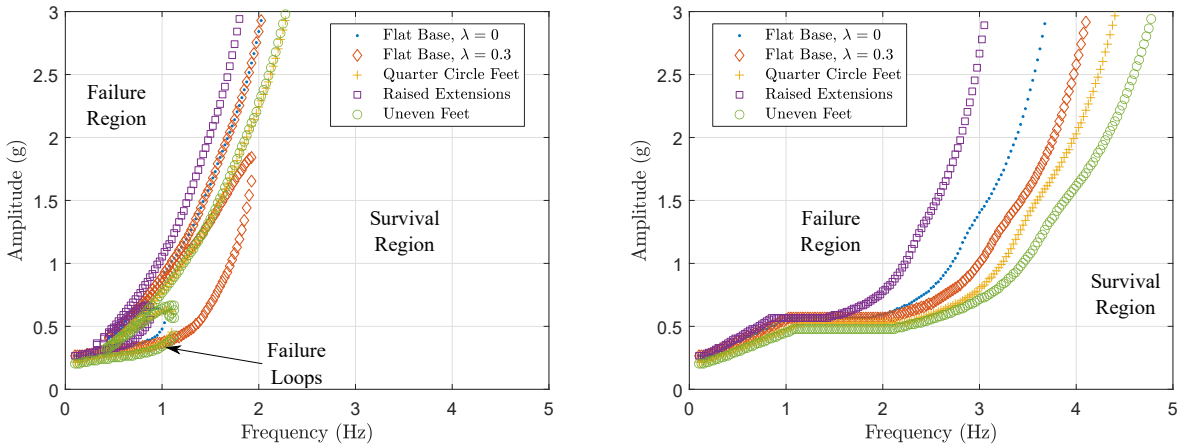

Fig. 16. Stability diagrams with boundaries between survival and failure marked. a) Initial positive (left) support acceleration. b) Initial negative (right) support acceleration.

The boundaries between survival and failure in a stability diagram are sensitive to the exact type of waveform used as shown in (Plaut et al. 1996). The results obtained from the stability diagrams cannot be generalized to other types of waveforms, and hence, only allow for qualitatively

discussing the importance of various effects on the response. For these simulations, $\mu = 0.55$ and $\epsilon = 0.1$, but any value could have been considered for these parameters. Additionally, the horizontal axis of Figure 16 gives the frequency in Hz of the sinusoidal pulse and the vertical axis gives the amplitude in g.

Several important conclusions can be drawn from observing the results shown in Figure 16. First, by comparing the stability diagram in Figure 16a and 16b for each type of base, the direction of the pulse matters due to the geometry of the object and its consequent location of c and moment of inertia. An initial negative support acceleration results in many more (f, A) pairs ending in failure compared to the opposite pulse direction. Another, important observation is that the different base configurations have a noticeably different stability diagram. Overall, the bases with uneven feet and quarter circle feet result in larger areas of failure in the stability diagram while the base with raised extensions fails for the least number of pulses. The difference in the minimum failure amplitude between different bases becomes more pronounced as the frequency increases.

The difference between the flat base with $\lambda = 0$ and $\lambda = 0.3$ is clear for both directions of the pulse, but particularly noticeable in the failure loops of Figure 16a where the loop for $\lambda = 0.3$ contains many more (f, A) pairs of failure than the loop for $\lambda = 0$. This is due to less energy being taken out of the base with $\lambda = 0.3$ during impacts and thus a greater amount of overturning when the pulse is reversed and the base impacts the support. There is no guarantee that λ would be zero for a flat base. Therefore, it is important to notice that using the usual assumption of $\lambda = 0$ for this base would result in non-conservative estimates for the stability of the body.

Finally, for either direction of pulse, the base with raised extensions (Figure 15c) proves to be the most stable overall. This is due not only to effectively widening the base through these extensions but also because an additional impact is caused that assists in reducing the energy of the body. The common case of a shelving unit with uneven feet proves to be least stable. While Figure 16 indicates that this case, which may arise from lack of fit or wear and tear on the feet, should be avoided. Hence, Figure 16 demonstrates that this case should be considered when studying the stability of such a system and that if a similar situation occurs the feet be replaced with a solution

that minimizes the potential problems caused by uneven feet.

Precariously Balanced Rock Subjected to Sinusoidal Pulses

Figure 17 shows an even more irregular body than the shelving unit: a scaled-down planar approximation of a PBR known colloquially as *Balanced Rock* located in Colorado (Jackson 1908). This rock was selected to show the model's potential to handle any irregular geometry and number of rocking vertices. It is reminded, however, that the study of the seismic risk of the original precariously balanced rock would require the study of its 3-D response to triaxial excitations which are more critical as shown in (Chatzis and Smyth 2012b), and hence the conclusions of this investigation should not be generalized to the risk of the original object. The real rock is nearly 11 meters tall, and has been scaled down so that experiments can be carried out in the future. The experimental body will be created by 3-D printing. An STL model of the body was produced by extrusion in the Z-direction. The STL for this body is provided in STL File S5 of the online supplementary material. The inclined support of the real PBR has been simplified to be horizontal to focus on the effect of the support accelerations on the system and simulate the case that will be used in the lab in the future. Throughout this example it is assumed that $\lambda = 0$.

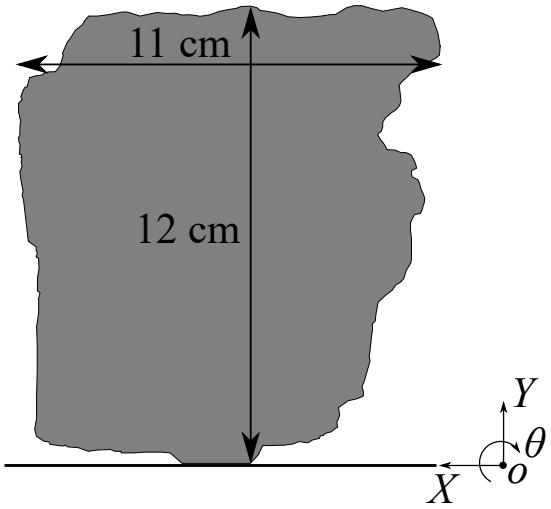

Fig. 17. A diagram showing the shape, dimensions, and coordinate system for the PBR studied.

In a similar manner as that for the shelving units, sinusoidal pulses are applied to the PBR to

examine the frequencies and amplitudes for which it survives and fails. For the PBR the angles -1.27 rad and 1.64 rad are selected to represent toppling in either direction.

Sinusoidal pulses varying A from $0.01g$ to $3g$ and f from 0.1 to 18 Hz were applied to the PBR. The survival and failure for each combination of the amplitude and frequency is converted into colored stability diagrams shown in Figure 18. For these simulations, $\mu = 0.75$ and $\epsilon = 0.1$. The red points correspond to pairs of (f, A) that result in overturning in the direction that the D'Alembert force acts for the first half of the pulse, f_{x0}, orange corresponds to failure in the opposite direction of the D'Alembert force, $-f_{x0}$, and white indicates survival for the pulse. The red, orange, and white regions will be referred to as failure A, failure B, and survival regions, respectively, through the rest of the paper.

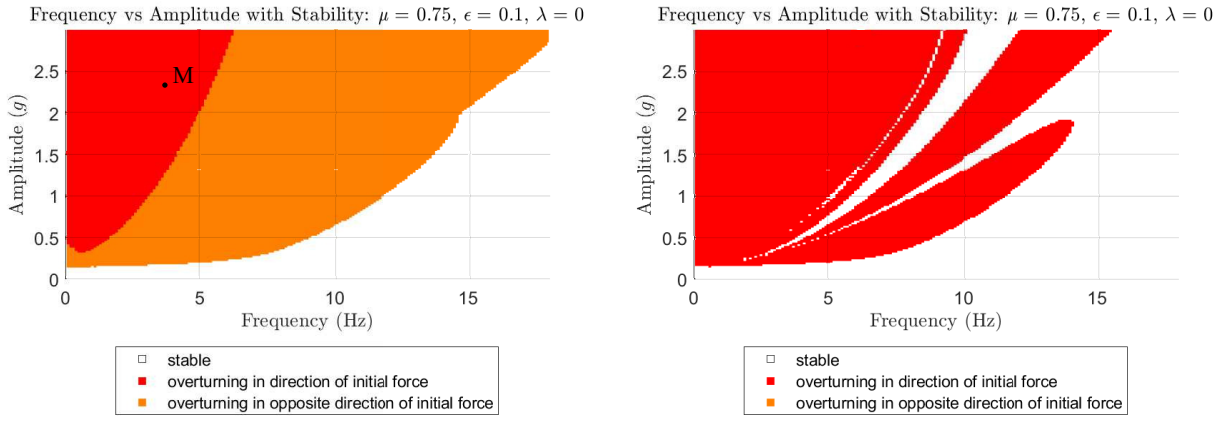

(a) **(b)**

Fig. 18. Stability diagrams for the PBR. (a) the results for an initial negative support acceleration; (b) the results for an initial positive support acceleration.

Figure 18a gives the results for an initial negative (right) support acceleration applied when the PBR is in the orientation shown in Figure 17 with the bottom edge flat on the support surface. The failure A region at low frequencies and high amplitudes shows failure by counterclockwise overturning. The failure B region that exists for all frequencies and only larger amplitudes as the frequency is increased, indicates clockwise toppling of the body. Finally, the survival region beneath a certain low amplitude indicates that the PBR does not overturn when the amplitude is

below a minimum threshold. This survival region extends upward for higher frequencies where the effect of the larger amplitudes is gradually undermined by the shorter duration of the pulse.

Figure 18b shows the stability results for an initial positive (left) support acceleration. As can be seen in the plot, the PBR either topples clockwise or survives. There are no counterclockwise failures when f_x initially acts to the right. Again, there is a minimum threshold for the amplitude below which the PBR does not fail that also extends upward as the frequency increases. Further, the solid failure A region for low frequencies and the lower failure A region that extends from the low frequencies upward are shapes analogous to stability diagrams produced for rectangular bodies. But alternating bands of survival and failure A are also visible for the PBR in Figure 18b. These bands result from the irregular geometry of the body and are not present for symmetric rectangular blocks under single-cycle support acceleration pulses (Zhang and Makris 2001).

Comparing Figures 18a and 18b proves the importance of geometry to the rocking response. Due to the shape of the PBR, it is much more likely to fail with clockwise rotation as large areas of $(f,\ A)$ pairs show this type of failure. This result is significant because it shows that pulses with identical frequency and amplitude applied to the same object can produce drastically different results when the pulse direction is changed.

In addition to the geometry, another important factor that contributes to the rocking response of the object is the value of μ. The following Figure 19 shows two stability plots for the PBR with a positive (left) initial support acceleration and all parameters the same except for μ.

The results for each μ are similar in that toppling only occurs in the clockwise direction and that similar areas of survival or failure are observed in both. It is important to note that for some frequencies nearing 15 Hz, the minimum amplitude which causes failure actually decreases for lower values of μ for which more sliding occurs. This corroborates the findings in (Chatzis and Smyth 2012a) and is an important result as ignoring sliding is often incorrectly assumed as a conservative assumption.

Figure 20 shows the time histories of the PBR for the pulse indicated by point M ($f = 3.5$ Hz, $A = 2.33g$) shown in Figure 18a.

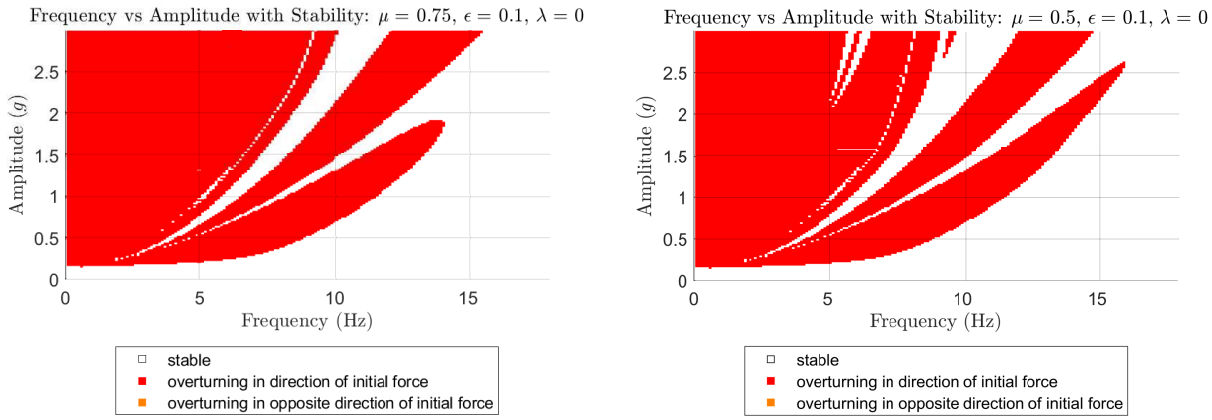

(a) **(b)**

Fig. 19. Stability diagrams for the PBR with initial positive (left) support acceleration for different coefficients of friction μ. (a) $\mu = 0.75$; (b) $\mu = 0.5$.

Two simulations were run to obtain the results of Figure 20. The blue line shows the counter-clockwise toppling failure of the PBR with $\mu = 0.75$. This is the time history indicated by point M in Figure 18a. The black line shows clockwise toppling failure for the same pulse and PBR, but for $\mu = 0.25$. A number of important observations are derived from these results. First, when μ is reduced from 0.75 to 0.25 the body exhibits a large amount of slide rocking as shown by $\dot{X}_{op}$ in Figure 20a: non-zero $\dot{X}_{op}$ indicates sliding of the rocking vertex for the black line. However, when the body has a higher μ, it experiences free flight. The lifting from the support can be seen in Figure 20b, showing the Y-position of the active rocking vertex. During intervals of free flight, this corresponds to the rocking vertex of the previous pattern. For $\mu = 0.75$ this vertex leaves the support at around 0.1 seconds. The body then fails as another corner hits the support. Note that the PBR with $\mu = 0.25$ does not exhibit free flight and fails in the opposite direction. This highlights the importance of considering both free flight and slide rocking in the model as a simple change of the coefficient of friction can result in free flight and a different type of failure. The motion of the PBR with $\mu = 0.75$ cannot be accurately described if free flight was ignored as a possible pattern. While this example shows that free flight occurs for the higher of the two μ considered, this is not always the case and often slide rocking is coupled with free flight as shown by (Chatzis and Smyth

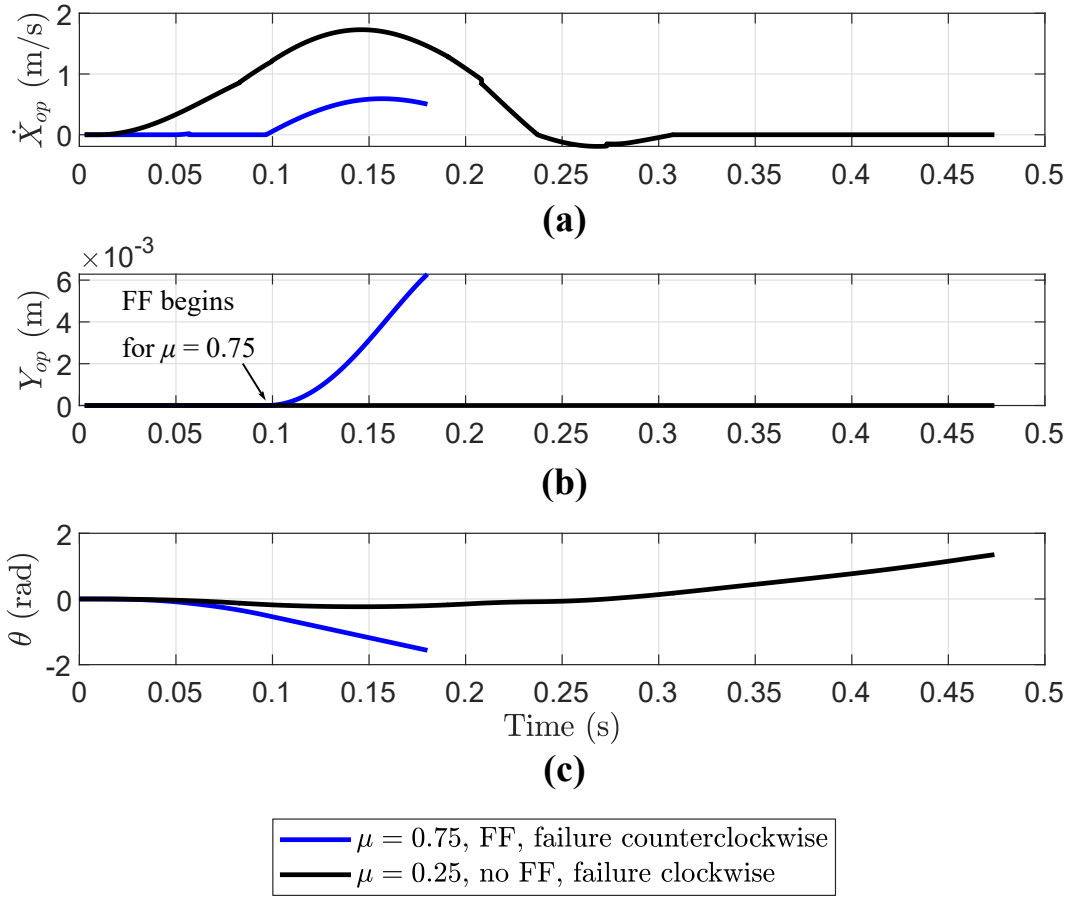

Fig. 20. Time histories of $\dot{X}_{op}$, Y_{op}, and θ for the PBR with the same pulse applied (point M from Figure 18a) but different μ. (a) The horizontal velocity $\dot{X}_{op}$ of the active rocking vertex. (b) The vertical position Y_{op} of the active rocking vertex (or the last rocking vertex in the case of free flight). (c) The angle θ of the body.

2012b). Additionally, while the examples of this paper do not show free flight occurring after an impact, this is also possible in which case the assumed value of ϵ would influence the response. Videos showing the movement of the PBR for these simulations are provided in the supplementary material. Videos for $\mu = 0.75$ at full speed and slow motion are provided in Videos S6 and S7 respectively. Full speed and slow motion videos for $\mu = 0.25$ are provided in Videos S8 and S9.

These results for the PBR show the importance of taking into account the object's irregular geometry, sliding, and free flight in a rocking model. One direction of the pulse can be more critical than its opposite for an irregular object and a lower μ, which results in more frequent occurrences

of sliding, can lead to more frequent failure. Finally, changes in the coefficient of friction can result in free flight and much different trajectories.

Museum Sculpture Subjected to an Earthquake

Michelangelo's famous Renaissance sculpture *David* was selected for a case study involving an earthquake. The original sculpture is located in Florence, Italy which is an area of high seismicity as demonstrated recently by the Galliano earthquake of December 2019. STL files of the sculpture were created in AutoCAD by drawing lines over the outline of an image of the sculpture (Michelangelo 1504). Similar to the previous example, the STL files are produced as a 2-D extrusion in the Z-direction with the face of the extrusion representing the front face of the sculpture. Nonetheless, one could have used the original 3-D geometry of the body and then taken its projection in the 2-D plane as discussed previously in relation to Figure 1. The original sculpture would be expected to experience planar rocking due to its rather elongated base. The investigation on a sculpture with extruded geometry is used in this example as it facilitates interesting discussions on the use of different base configurations. Two geometries are considered as shown in Figure 21, with and without a rectangular pedestal on the base of the sculpture denoted by points a, b, c, and d in the figure. Several pedestal configurations: solid, hollow, chamfer, and solid with feet are created to test the effect of the pedestal's mass and the number of rocking vertices engaged. STL files for each configuration of the *David* studied are provided in the supplemental material for this paper as follows: no pedestal: STL File S10; solid pedestal: STL File S11; hollow pedestal: STL File S12; chamfered pedestal: STL File S13; and solid pedestal with feet: STL File S14. Note that the triangular feet added to the solid pedestal have negligible size and mass and this base configuration practically responds the same as the solid pedestal with $\lambda = 0$. These files were imported into Matlab to test the response of the bodies to the support accelerations recorded during an earthquake that struck Rocchetta, Italy in October 2016. The support accelerations for this earthquake were downloaded from the Orfeus Engineering Strong Motion Database (Luzi et al. 2015) and the file was trimmed to include the data points numbered 6336 to 10334. The resulting accelerations are plotted in Figure 22.

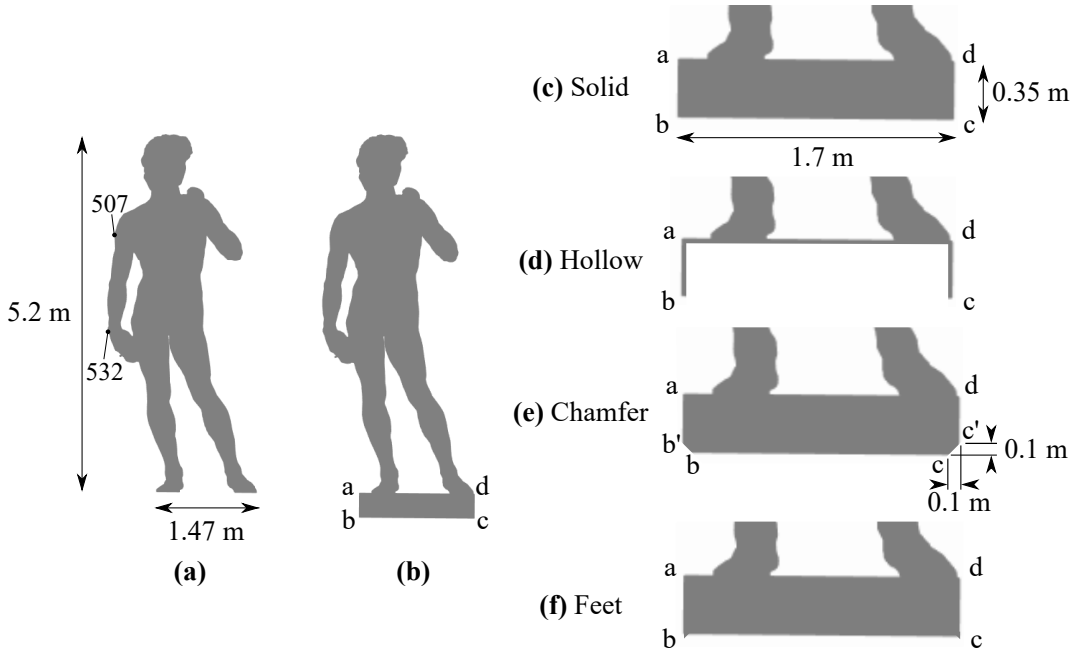

Fig. 21. Representations of Michelangelo's *David*. (a) The sculpture without a pedestal; (b) the sculpture with a solid pedestal; (c) a detail of the solid pedestal; (d) a detail of the hollow pedestal; (e) a detail of the chamfered pedestal; (f) a detail of the solid pedestal with small triangular feet at b and c.

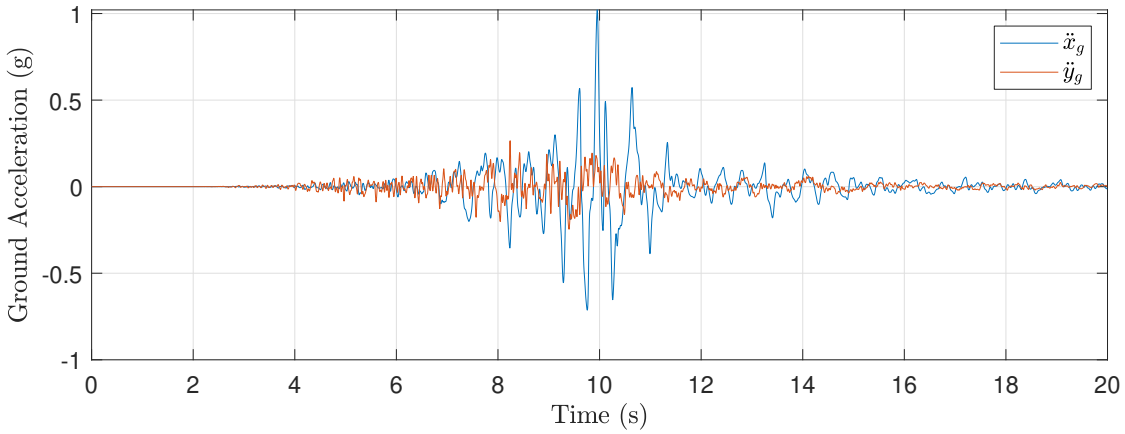

Fig. 22. Support accelerations from the Rocchetta, Italy earthquake in October 2016.

The sculpture was modelled as 5.2 meters from bottom of foot to top of head, corresponding to the real dimensions of the sculpture. The pedestal is 1.7 meters by 0.35 meters. $\mu = 0.5$ to model the marble sculpture in contact with a marble support and the density of the sculpture is set to the density of marble, 2711 kg/m^3. The vertical accelerations and the horizontal accelerations from

one of the horizontal directions of the earthquake were applied to each of the sculptures.

Figure 23 shows the time histories after six seconds, as the body remains in the static pattern before this, for each state in $\boldsymbol{Q}$ of the *David* without any pedestal and $\lambda = 0$ when subjected to the earthquake. The object fails by counterclockwise rotation after making many impacts (denoted by red circles in Figure 23) and a transition from pure rocking to slide rocking just before failure (indicated by the red asterisk and "SR" label). The model produces results for all states but the time history for θ is most informative as failure is defined by two angles of θ. A video of the dynamics of the *David* without a pedestal during the Rocchetta earthquake is provided in Video S15 in the supplementary material.

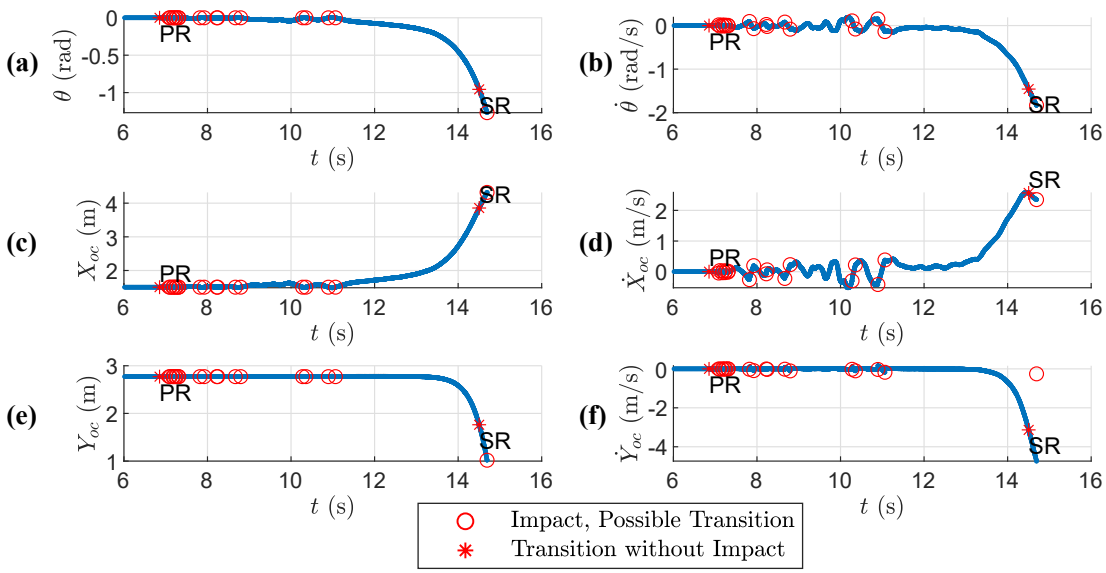

Fig. 23. The time histories of each state of $\boldsymbol{Q}$ for the *David* without a pedestal and $\mu = 0.5$, $\epsilon = 0.1$, and $\lambda = 0$. (a) θ; (b) $\dot{\theta}$; (c) X_{oc}; (d) Y_{oc}; (e) $\dot{X}_{oc}$; (f) $\dot{Y}_{oc}$. The labels PR and SR on the time histories correspond to the beginning of pure rocking and slide rocking, respectively.

The responses of different base configurations are tested under the same Rochetta earthquake. Figure 24 shows the time history after six seconds for θ for the configurations with no pedestal, the solid pedestal with $\lambda = 0$, and the hollow pedestal. For both pedestal configurations, the body is fixed on the pedestal and the pedestal is free-standing on the support medium.

The sculpture with the solid pedestal survives the Rocchetta earthquake while the sculpture with

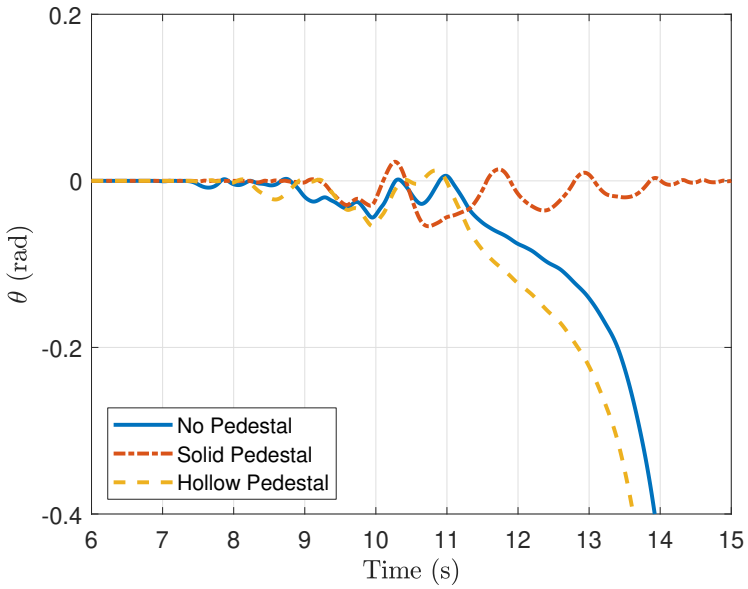

Fig. 24. The time histories of θ for the *David* with no pedestal, the solid pedestal with $\lambda = 0$, and the hollow pedestal.

the hollow pedestal fails in a similar manner as the sculpture with no pedestal. Thus, the addition of the solid pedestal might affect the response of such a body significantly during the earthquake. The survival of the sculpture with the solid pedestal is attributed to the lowering of the center of mass of the object by the addition of mass on the base of the sculpture. The sculpture with the hollow pedestal results in failure in the same direction and around the same time as the sculpture without a pedestal. This shows that increasing the width of the base and overall height of the sculpture does not keep the sculpture from overturning as an addition of mass to the base does. Given the stochastic nature of earthquake accelerations, another time history with different record properties could yield a different result when applied to the same base configurations of the David and might even result in overturning failure where survival occurs for another earthquake. In light of this, a full analysis of the seismic risk of irregular objects such as sculptures would require a study with a number of earthquakes to accurately determine their risk of overturning (Garcia Espinosa 2017).

Museum Sculpture Subjected to Sinusoidal Pulses

Figure 25 shows the stability diagram boundaries for sinusoidal pulses for the five configurations of the *David* shown in Figure 21: without any pedestal, with the solid pedestal and $\lambda = 0$, with the

solid pedestal and $\lambda = 0.15$, with the chamfered pedestal and $\lambda = 0$, and with the hollow pedestal and $\lambda = 0$. When the body has a concave portion between its rocking vertices as the hollow pedestal does, $\lambda = 0$ is most appropriate. However, if there is a solid portion between the rocking vertices as for the solid pedestal, λ may be greater than zero and thus two values of λ are tested in this example. The chamfered pedestal could also reasonably have $\lambda > 0$ but this study examines the effect of a change in the number of rocking vertices by way of the chamfered pedestal and keeps $\lambda = 0$ so that the responses for different pedestals are more easily compared to each other.

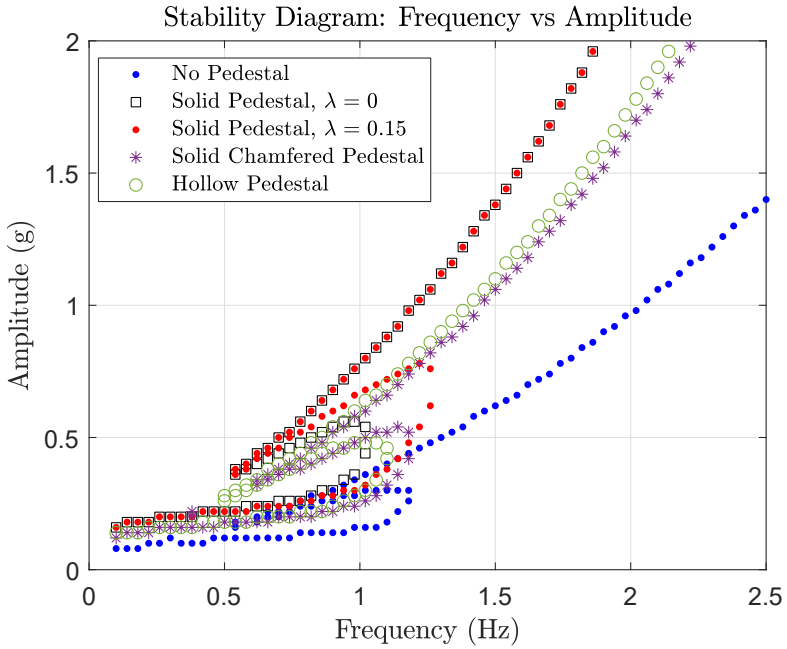

Fig. 25. A diagram showing the survival and failure boundaries for the various base conditions of the *David* sculpture.

As demonstrated in Figure 25, when λ is increased, the sculpture topples more frequently after impact. Each base configuration exhibits an overturning "loop" where the sculpture's base experiences impacts with the support before failing. This loop for $\lambda = 0.15$ in Figure 25 is considerably larger than that for the solid pedestal with $\lambda = 0$, but the boundary between survival and failure outside of the loop is identical regardless of λ because the body topples without impact between its initial support contacts, thus making λ inapplicable for those pulses. Because the pedestal with $\lambda = 0.15$ results in failure for pairs of (f, A) for which the body would have survived

with the solid pedestal with $\lambda = 0$, assuming $\lambda = 0$ is not conservative as also shown in (Chatzis et al. 2017).

There are clear differences between the stability diagrams without the pedestal and with the pedestal. The sculpture without its pedestal has a much lower minimum threshold for failure amplitude at all frequencies with the difference increasing as f increases. The solid pedestals are beneficial in preventing the toppling of the sculpture. As shown in the previous example, this is due to the extra mass on the bottom of the sculpture which lowers the center of mass of the sculpture and also slightly increases the distance between the sculpture's support contacts, thus also increasing the moment arm that must be overcome to topple the sculpture.

The results for the hollow pedestal show an intermediate result between the two solid pedestal configurations. The failure amplitude is less for the hollow pedestal for all frequencies when compared to the solid pedestal with $\lambda = 0$, but the relationship is more complicated when compared to $\lambda = 0.15$. In this case, the hollow pedestal generally fails at a lower amplitude except for a region around 1.1 to 1.3 Hz. The hollow pedestal still has better resistance to overturning than no pedestal in all instances. Thus, adding a pedestal to the body despite it raising the body's center of mass, even if the pedestal is hollow, can increase the object's resistance to overturning but this configuration still performs poorly compared to a solid pedestal, particularly when $\lambda = 0$, which can be obtained in practice by placing small "feet" at the rocking vertices of the pedestal to ensure the impulse is applied at the vertex. A flat pedestal without feet should conservatively be assumed to have $\lambda \geq 0.15$.

Finally, the sculpture with the chamfered pedestal has an interesting result when compared to the other configurations. The chamfered pedestal generally provides better resistance to overturning compared to no pedestal but has a larger region of (f, A) pairs which result in failure. The chamfered pedestal with $\lambda = 0$ shows less resistance to overturning compared to the solid pedestal with $\lambda = 0$ which indicates that the chosen chamfered geometry does not improve the overturning stability. This is most likely due to the narrower base of the chamfered pedestal and the fact that X_{oc} is not bounded by the X-coordinates of the vertices in contact with the support at impact. For

example, X_{oc} is not bounded by X_{ob} and $X_{ob'}$ when the body rotates to impact at b′ as shown in Figure 21 thus making the body unstable at this rotation. However, it is possible that there is an optimal chamfer angle and width that would result in greater rocking stability if the energy of the body can be reduced through this additional impact and the centroid kept above the outer vertices of the base.

These results show that using a solid pedestal with the minimum value of $\lambda = 0$ for an irregular body is most preferable for rocking stability. This value for λ can be achieved practically by the implementation of feet on the outer edges of the body's pedestal to limit the components of the vertical impulse on portions of a flat pedestal between the support contacts. The addition of feet drastically reduces the area of (f, A) pairs resulting in failure when compared to the solid pedestal with a reasonable $\lambda = 0.15$. The addition of feet also increases the minimum failure amplitude for many pulses. However, if a solid pedestal cannot be obtained, the addition of a hollow pedestal can still improve the object's resistance to overturning.

Terracotta Warrior Subjected to Sinusoidal Pulses

For the terracotta warrior shown in Figure 26, the full 3-D geometry of the sculpture is used to calculate its mass and moment of inertia and the 2-D projection of the rectangular base is combined with this data to create a body that will produce a planar response. The body can be assumed to experience planar rocking under several scenarios: because its base is elongated in the out-of-plane direction, because it is mechanically constrained, or, commonly in the literature, by assuming that the excitation is only applied in the XY plane and that the Z-coordinate of the centroid of the body and the rectangular pedestal on which the sculpture is placed are the same. This model focuses on the effect of using an accurate mass moment of inertia for this object, opposed to the moment of inertia for an approximate rectangular block, and studies the effects of the geometry, sliding and free flight in the planar rocking response of this object.

of one of the terracotta warriors from the Terracotta Army in Shaanxi, China (shown in Figure 26a and 26b) was selected for testing. The model of the body has approximate dimensions of 3.5 m high by 1.2 m wide by 1.2 m deep at its greatest sections while the pedestal is a rectangular

prism with dimensions 0.8 m by 0.8 m by 0.1 m. The densities of both the body and pedestal are equal. The centroid (and geometric center consequently) of the pedestal is initially aligned with the centroid of the body without the pedestal and they are rigidly fixed to each other. The moment of inertia is calculated about c. The actual sculpture rests on soil and $\mu = 0.5$ is selected to approximate the contact between terracotta and soil while the soil is assumed to be sufficiently rigid. The effect of an eccentric base configuration is tested for this model by moving the base in the positive X-direction relative to the body of the sculpture by 1% of the total base width (0.008 m) as depicted in Figure 26c. This causes the overall centroid of the rigid body to be slightly closer to the right vertex of the base. Stability diagrams for this object are provided in Figure 27.

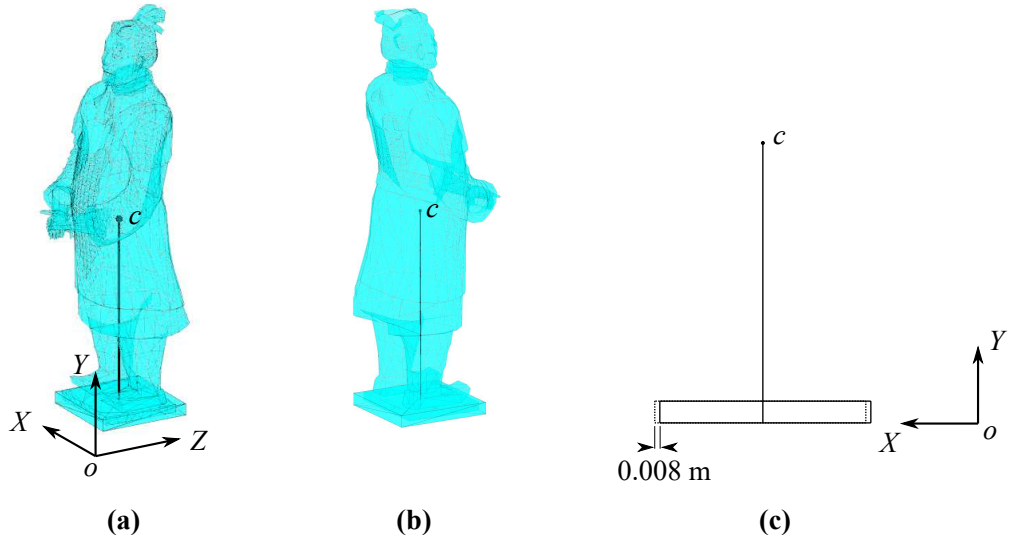

Fig. 26. An STL representation of a terracotta warrior from Shaanxi, China. (a) a front view of the sculpture with the body's centroid vertically aligned with the centroid and geometric center of the pedestal; (b) a rear view of the sculpture; (c) a depiction of the eccentricity of 0.008 m applied to the pedestal. The dashed and solid lines correspond to the outline of the centered and 0.008 m offset pedestal respectively.

Figure 27a shows the results of the centered pedestal with $\lambda = 0$. There is a large failure A region which does not extend past 4 Hz for all realistic amplitudes of acceleration. In addition, there is a small failure B region. Because the centroid is above the geometric center of the pedestal in this case and the base of the body that contacts the support is symmetric about the centroid, sinusoidal pulses in the opposite direction yield the same stability diagram. On the other hand,

Figure 27b and 27c shows the results for the body with the eccentric base.

The same pulses applied to the centered body in Figure 27a are applied for the eccentric base configuration where 27b and 27c correspond to positive and negative initial support accelerations respectively. Drastic changes in the stability diagram are observed in Figure 27b. The failure A region remains essentially the same, but the failure B region grows dramatically, signifying a much higher susceptibility to failure with impact due to the eccentricity of the body. The body experiences slide rocking and pure rocking and fails by overturning about the rocking vertex nearer the centroid as might be expected. As the body is asymmetric, pulses in the opposite direction reap a unique response as well. As the support acceleration now causes the body to rotate about the rocking vertex nearer the centroid before impact, the failure A region actually increases slightly, extending past 4 Hz where it did not previously. On the other side, the failure B region decreases in size, indicating greater safety if the object does not topple without impact. This is presumably due to the greater distance on the left side between the centroid and the rocking vertex which causes a greater reduction in energy than for the right side at impact. The right side also provides less resistance to overturning during integration of the post-impact rocking pattern due to the smaller effective width of the right side of the base compared to the left.

These results prove the critical importance of the location of the centroid in relation to the base geometry of the object. If the location of the body's centroid is changed by only 1% of the base width horizontally, the body's regions of survival and failure can change greatly. For pulses in one direction, there are many more pairs of amplitudes and frequencies that would cause the body to fail than the centered body but for pulses in the opposite direction, the object has a slightly smaller failure A region. Overall, as the direction of seismic or other forms of support accelerations cannot be chosen by those with interest in protecting at-risk objects, the large increase in the failure region exhibited in Figure 27c makes any eccentricity in such objects more susceptible to failure than those with no eccentricity.

As in the case of the PBR in the first example, it is also important to note the importance of sliding in the dynamic response of the terracotta warrior during the sine pulses. The plot in Figure

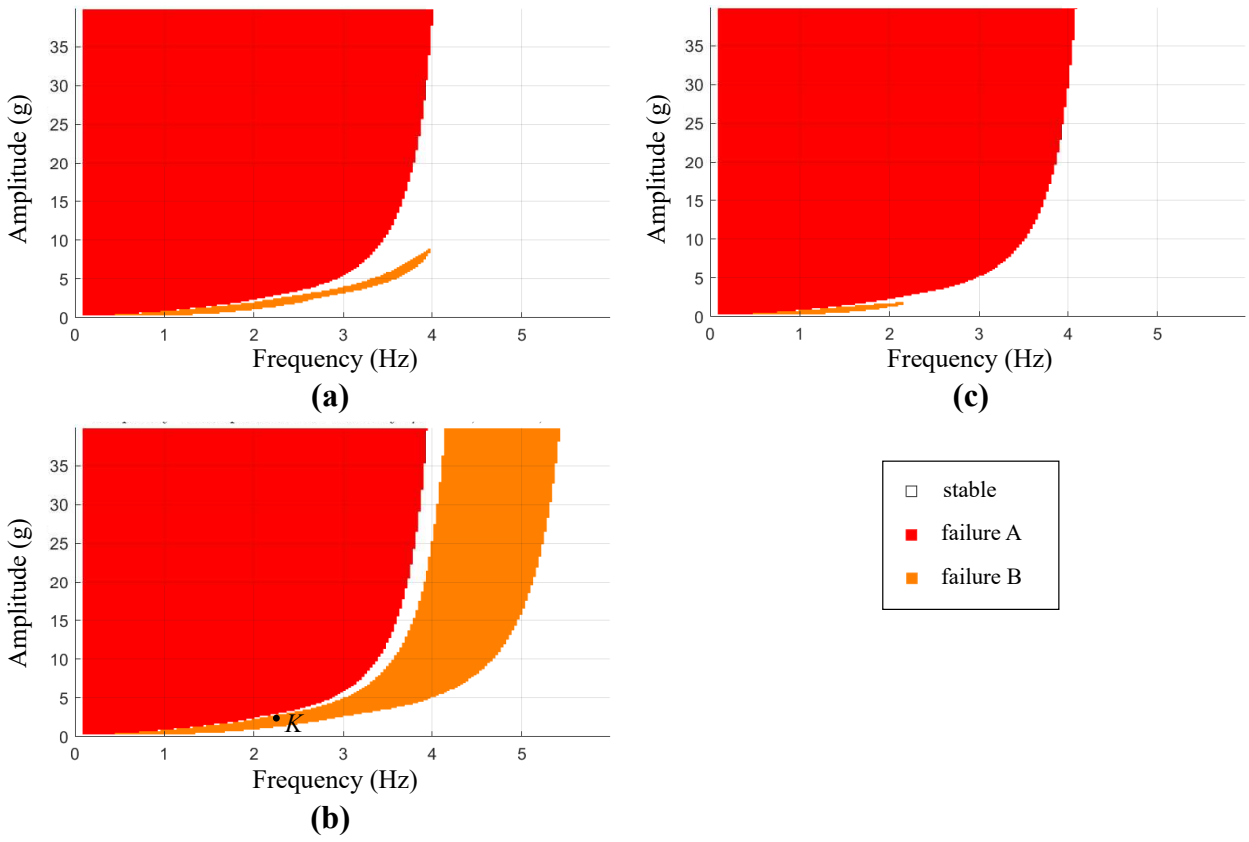

Fig. 27. Stability diagrams for the terracotta warrior sculpture with $\lambda = 0$. (a) no eccentricity; (b) 1% eccentricity and an initial positive support acceleration; (c) 1% eccentricity and an initial negative support acceleration.

28 shows X_{op} and $\dot{X}_{op}$ where p is the active rocking vertex, and the pulse applied is the (f, A) pair corresponding to point K from the stability diagram of Figure 27c. The non-zero values for $\dot{X}_{op}$ indicate that the object is in slide rocking before overturning. Slide rocking occurs for many pulses which result in failure in Figure 27. Point K is a mild example as many pulses result in drastic sliding even with a $\mu = 0.5$, which is normally considered as high. The instability arising from sliding is further evidence that neglecting sliding is not conservative for irregular objects in planar rocking.

Further, as researchers have found the 3-D non-planar rocking of objects to be nonconservative (Chatzis and Smyth 2012a; Zulli et al. 2012; Egidio et al. 2014), future studies should not be restricted to the planar motion of such objects.

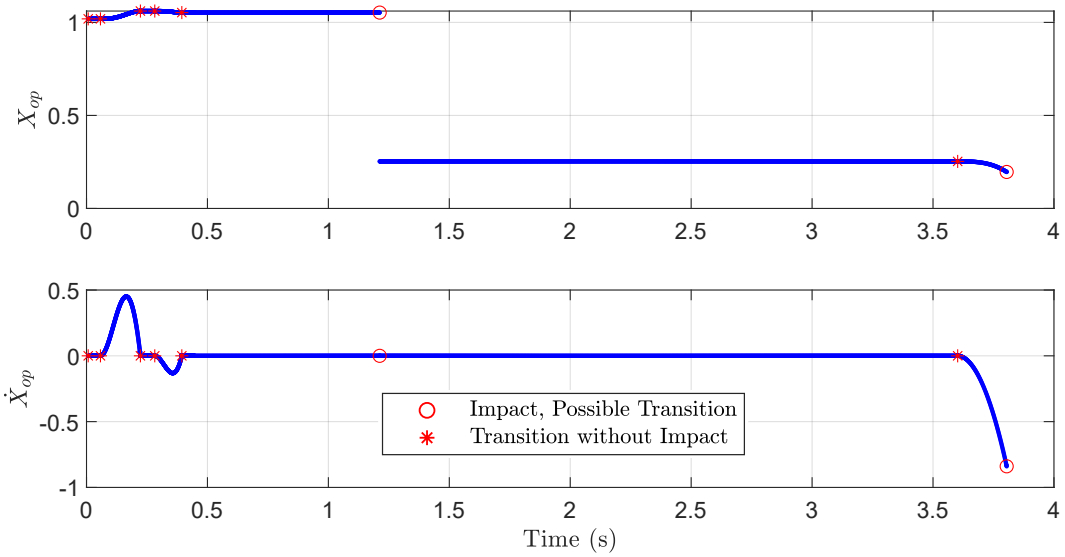

Fig. 28. The time history for the active rocking vertex horizontal position and velocity, X_{op} and $\dot{X}_{op}$, for point K from Figure 27 showing slide rocking leading to failure.

CONCLUSIONS

A model for examining the planar rocking behavior of an irregular body with any polygonal geometry is introduced in this paper. The model takes into account sliding, free flight, and the variable location of the impulse at impact defined by λ. It also allows for the examination of any rigid body given only the STL file defining the geometry of the body and the desired support accelerations to be applied to it. This new model allows for studying the response of a body with any in-plane geometry and any number of potential rocking vertices. Newtonian equations of motion for the non-linear system were formulated in an automated manner and solved using Matlab's symbolic toolbox, ode45, and ODE event location functionality. Equations of momentum for impacts were also formulated and solved taking into account sliding and free flight due to impact.

This model can be considered as an extension of the Shenton and Jones model (Shenton III and Jones 1991) for bodies that are not symmetric, are non-rectangular, and have multiple rocking vertices. It can be used by the reader for many systems that could not have been studied previously in the literature. The examples present several cases which demonstrate that the geometry of the body and its base configuration, the value of μ, the location of the vertical impulse defined by λ,

the direction of the pulse, the presence of sliding and free flight, and the eccentricity of the centroid relative to its support contacts are all critical to determining the accurate rocking response of an irregular body.

The effect of the different base configurations is demonstrated through the example of the shelving unit, a common item typically designed by non-experts in dynamics. The designer of the base configuration in such a case would normally only consider the aesthetic or other practical factors when designing the base, but it has been shown that the effect of the base on the dynamic response should be considered as it can have a significant effect on the stability of the system. The studies on the PBR further show the importance of using the full irregular geometry as different directions of failure are not equally common as for a rectangular block. Further, it verifies past results demonstrated by the authors where neglecting sliding is not a conservative assumption (Chatzis and Smyth 2012b). The study on Michelangelo's sculpture with various base configurations shows the importance of accounting for a variable λ or trying to control it through modifying the base of the sculpture, showing that a solid pedestal with $\lambda = 0$, which can be achieved through small feet at the vertices, is most beneficial for the rocking stability of this sculpture. Finally, the terracotta warrior example shows the importance of minimizing the eccentricity between the centroid of the sculpture and geometric center of the base as well as the unstable nature of the object due to sliding. Particular findings of note are the abnormal shapes in the stability diagram that are not present for symmetric rectangular bodies subject to sine pulses and the finding that permitting more sliding by reducing μ does not result in a more stable body.

The software that utilizes this model will be useful for studying the effects of earthquakes and other support accelerations on objects such as museum artifacts, PBRs, and other objects susceptible to rocking under conditions that would result in those objects experiencing planar rocking. As stated in the introduction, the model is capable of handling curved geometries as in Figure 1d through their polygonal approximations, a topic which has been studied in (Burton and Chatzis 2021) and will be the focus of a future paper from the authors. The examples presented focus on irregular geometries that substantially deviate from a simple rectangular geometry; however, this model also

enables the study of geometric defects of any shape or size. Finally, this paper has demonstrated the importance of accounting for the irregular geometry of a rocking body under conditions that would reasonably result in a planar response. Nonetheless, more general 3-D irregular geometries of many bodies would not result in planar rocking. In such cases, neglecting the 3-D nature of the response is not a conservative assumption (Chatzis and Smyth 2012a; Zulli et al. 2012). As such, the extension of this model to 3-D is an important research step to take. This work, and the automated procedure suggested for formulating the equations of motion, defining the transitions between patterns, and solving the momentum equations, facilitates such an extension.

Data Availability Statement

- Some or all data, models, or code that support the findings of this study are available from the corresponding author upon reasonable request. All input data to the models have been made available to the user. The output data have been presented in figures in the paper but can be made available upon reasonable request. All models used for the studies have been fully described in the paper.

Acknowledgments

The authors thank the Clarendon Fund for providing funding to the first author for this research.

SUPPLEMENTAL MATERIALS

The videos and STL files S1–S15 are available online in the ASCE Library (ascelibrary.org).

REFERENCES

Abadi, H. A., Paton-Cole, V., Gad, E., Lam, N., and Patel, V. (2017). "Rocking behavior of irregular free-standing objects subjected to earthquake motion." *Journal of Earthquake Engineering*, 23(5), 793–809.

Acikgoz, S. and DeJong, M. J. (2012). "The interaction of elasticity and rocking in flexible structures allowed to uplift." *Earthquake Engineering & Structural Dynamics*, 1–18.

Arredondo, C., Jaimes, M. A., and Reinoso, E. (2017). "A simplified model to evaluate the dynamic rocking behavior of irregular free-standing rigid bodies calibrated with experimental shaking-table tests." *Journal of Earthquake Engineering*, 23(1), 46–71.

Boroschek, R. and Romo, D. (2004). "Overturning criteria for non-anchored non-symmetric rigid bodies." *Proceeding of the 13th world conference on earthquake engineering*, 1–6.

Brune, J., Purvance, M., and Anooshehpoor, A. (2007). "Gauging earthquake hazards with precariously balanced rocks." *American Scientist*, 95(1), 36.

Burton, M. D. and Chatzis, M. N. (2021). "Investigating the rocking dynamics of rigid right prisms with regular polygonal bases." *17th World Conference on Earthquake Engineering, 17WCEE, Sendai, Japan*.

Chatzis, M., Espinosa, M. G., and Smyth, A. (2017). "Examining the energy loss in the inverted pendulum model for rocking bodies." *Journal of Engineering Mechanics*, 143(5), 04017013.

Chatzis, M., Garcia Espinosa, M., Needham, C., and Williams, M. (2018). "Energy loss in systems of stacked rocking bodies." *Journal of Engineering Mechanics*, 144.

Chatzis, M. and Smyth, A. (2012a). "Modeling of the 3d rocking problem." *International Journal of Non-Linear Mechanics*, 47(4), 85–98.

Chatzis, M. and Smyth, A. (2012b). "Robust modeling of the rocking problem." *Journal of Engineering Mechanics*, 138, 247–262.

Chatzis, M. N. and Smyth, A. W. (2013). "Three-dimensional dynamics of a rigid body with wheels on a moving base." *Journal of Engineering Mechanics*, 139(4), 496–511.

Dimitrakopoulos, E. G. and DeJong, M. J. (2012). "Revisiting the rocking block: closed-form

solutions and similarity laws." *Proceedings of the Royal Society A: Mathematical, Physical and Engineering Sciences*, 468(2144), 2294–2318.

Dormand, J. and Prince, P. (1980). "A family of embedded runge-kutta formulae." *Journal of Computational and Applied Mathematics*, 6(1), 19–26.

Eberly, D. (2009). "Polyhedral mass properties (revisited) (https://www.geometrictools.com/documentation/documentation.html).

Egidio, A. D., Zulli, D., and Contento, A. (2014). "Comparison between the seismic response of 2d and 3d models of rigid blocks." *Earthquake Engineering and Engineering Vibration*, 13(1), 151–162.

Esmonde-White, F. (2011). "Patch slim (patchslim.m)." *MATLAB Central File Exchange*.

Fragiadakis, M., DiSarno, L., Saetta, A., Castellano, M. G., Rocca, I., Diamantopoulos, S., Crozet, V., Politopoulos, I., Chaudat, T., Vasic, S., Bal, I., Smyrou, E., Psycharis, I., Hutchinson, T., and Berto, L. (2020). "EXPERIMENTAL SEISMIC ASSESSMENT AND PROTECTION OF MUSEUM ARTEFACTS.

Garcia Espinosa, M.; Chatzis, M. (2017). "A preliminary investigation of methods for estimating theprobability of failure for rocking bodies." *16th World Conference on Earthquake, 16WCEE 2017*, <http://wcee.nicee.org/wcee/article/16WCEE/WCEE2017-3778.pdf>.

Godin, G., Beraldin, J.-A., Taylor, J., Cournoyer, L., Rioux, M., El-Hakim, S., Baribeau, R., Blais, F., Boulanger, P., Domey, J., and Picard, M. (2002). "Active optical 3d imaging for heritage applications." *IEEE Computer Graphics and Applications*, 22(5), 24–35.

Housner, G. W. (1963). "The behavior of inverted pendulum structures during earthquakes." *Bulletin of the Seismological Society of America*, 53(2), 403–417.

Ishiyama, Y. (1982). "Motions of rigid bodies and criteria for overturning by earthquake excitations." *Earthquake Engineering & Structural Dynamics*, 10(5), 635–650.

Jackson, W. H. (1908). "Balanced rock, garden of the gods, colorado (https://www.dia.org/art/collection/object/balanced-rock-garden-gods-87825)." Detroit Publishing Co.

Johnson, E. (2011). "Stl file reader." *MATLAB Central File Exchange*.

Koh, A.-S. and Mustafa, G. (1990). "Free rocking of cylindrical structures." *Journal of Engineering Mechanics*, 116(1), 35–54.

Koh, A.-S., Spanos, P. D., and Roesset, J. M. (1986). "Harmonic rocking of rigid block on flexible foundation." *Journal of Engineering Mechanics*, 112(11), 1165–1180.

Luzi, L., Puglia, R., Russo, E., and ORFEUS Working Group 5 (2015). "Engineering strong motion database (esm).

MathWorks (2019a). "matlabfunction (https://www.mathworks.com/help/symbolic/matlabfunction.html)." *MathWorks.com*.

MathWorks (2019b). "Symbolic math toolbox (https://www.mathworks.com/products/symbolic.html)." *MathWorks.com*.

Michelangelo (1501-1504). "David (https://commons.wikimedia.org/wiki/file:Jorg Bittner Unna, Wikimedia Commons.

of Congress, U. L. (2019). "Stl (stereolithography) file format, binary (https://www.loc.gov/preservation/digital/formats/fdd/fdd000505.shtml)." *Sustainability of Digital Formats: Planning for Library of Congress Collections*.

Plaut, R., Fielder, W., and Virgin, L. (1996). "Fractal behavior of an asymmetric rigid block overturning due to harmonic motion of a tilted foundation." *Chaos, Solitons & Fractals*, 7(2), 177–196.

Psycharis, I. N. and Jennings, P. C. (1983). "Rocking of slender rigid bodies allowed to uplift." *Earthquake Engineering & Structural Dynamics*, 11(1), 57–76.

R. Lipscombe, P. and Pellegrino, S. (1993). "Free rocking of prismatic blocks." *Journal of Engineering Mechanics*, 119, 1387–1410.

Semechko, A. (2019). "Rigid body parameters of closed surface meshes (https://www.github.com/antonsemechko/rigid-body-parameters)." *GitHub*.

Shampine, L. F. and Gordon, M. K. (1975). *Computer solution of ordinary differential equations: the initial value problem*. Freeman, San Francisco, CA, <http://cds.cern.ch/record/105968>.

Shenton III, H. W. and Jones, N. P. (1991). "Base excitation of rigid bodies. i: Formulation." *Journal of Engineering Mechanics*, 117(10), 2286–2306.

Shi, B., Anooshehpoor, A., Zeng, Y., and N Brune, J. (1996). "Rocking and overturning of precariously balanced rocks by earthquakes." *Bulletin of the Seismological Society of America*, 86.

Spanos, P. D. and Koh, A.-S. (1984). "Rocking of rigid blocks due to harmonic shaking." *Journal of Engineering Mechanics*, 110(11), 1627–1642.

Spyrakos, C. C., Maniatakis, C. A., and Taflampas, I. M. (2017). "Application of predictive models to assess failure of museum artifacts under seismic loads." *Journal of Cultural Heritage*, 23, 11–21.

Srinivasan, M. and Ruina, A. (2008). "Rocking and rolling: A can that appears to rock might actually roll." *Phys. Rev. E*, 78, 066609.

The Mathworks, I. *atan2*. https://uk.mathworks.com/help/matlab/ref/atan2.html, <https://uk.mathworks.com/help/matlab/ref/atan2.html>.

Tso, W. K. and Wong, C. M. (1989). "Steady state rocking response of rigid blocks part 1: Analysis." *Earthquake Engineering & Structural Dynamics*, 18(1), 89–106.

Várkonyi, P. L., Kocsis, M., and Ther, T. (2021). "Rigid impacts of three-dimensional rocking structures." *Nonlinear Dynamics*.

Voyagaki, E., Psycharis, I. N., and Mylonakis, G. (2014). "Complex response of a rocking block to a full-cycle pulse." *Journal of Engineering Mechanics*, 140(6), 04014024.

Weisstein, E. W. (2019). "Convex hull (https://demonstrations.wolfram.com/convexhull/)." *From MathWorld–A Wolfram Web Resource.*

Wittich, C. E., Hutchinson, T. C., Wood, R. L., Seracini, M., and Kuester, F. (2016). "Characterization of full-scale, human-form, culturally important statues: Case study." *Journal of Computing in Civil Engineering*, 30(3), 05015001.

Yim, C.-S. and Chopra, A. K. (1984). "Earthquake response of structures with partial uplift on winkler foundation." *Earthquake Engineering & Structural Dynamics*, 12(2), 263–281.

Yim, C.-S., Chopra, A. K., and Penzien, J. (1980). "Rocking response of rigid blocks to earthquakes." *Earthquake Engineering & Structural Dynamics*, 8(6), 565–587.

Yim, S. C. S. and Lin, H. (1991). "Nonlinear impact and chaotic response of slender rocking objects." *Journal of Engineering Mechanics*, 117(9), 2079–2100.

Zhang, J. and Makris, N. (2001). "Rocking response of free-standing blocks under cycloidal pulses." *Journal of Engineering Mechanics*, 127(5), 473–483.

Zulli, D., Contento, A., and Egidio, A. D. (2012). "3d model of rigid block with a rectangular base subject to pulse-type excitation." *International Journal of Non-Linear Mechanics*, 47(6), 679–687.